UNIVERSITY OF BIRMINGHAM

University of Birmingham Research at Birmingham

In situ neutron diffraction unravels deformation mechanisms of a strong and ductile FeCrNi medium entropy alloy

Tang, Lei; Jiang, F. Q. ; Wróbel, J. S.; Liu, B.; Kabra, S.; Duan, R. X. ; Luan, J. H.; Jiao, Z. B. ; Attallah, Moataz; Nguyen-Manh, D.; Cai, Biao

Link to publication on Research at Birmingham portal

In Situ Neutron Diffraction Unravels Deformation Mechanisms of a Strong and Ductile FeCrNi Medium Entropy Alloy

L. Tang[a], F.Q. Jiang[b], J.S. Wróbel[c], B. Liu[d], S. Kabra[e], R.X. Duan[a], J.H. Luan[f], Z.B. Jiao[g], M.M. Attallah[a], D. Nguyen-Manh[h**], B. Cai[a*]

[a] School of Metallurgy and Materials, University of Birmingham, B15 2TT, United Kingdom
[b] Shenyang National Laboratory for Materials Science, Institute of Metal Research, Chinese Academy of Sciences, Shenyang 110016, China
[c] Faculty of Materials Science and Engineering, Warsaw University of Technology, ul. Wołoska 141, 02-507 Warsaw, Poland
[d] State Key Laboratory for Powder Metallurgy, Central South University, 410083, PR China
[e] ISIS Facility, Rutherford Appleton Laboratory, Didcot OX11 0QX, United Kingdom
[f] Department of Materials Science and Engineering, City University of Hong Kong, Hong Kong, China
[g] Department of Mechanical Engineering, The Hong Kong Polytechnic University, Hong Kong, China
[h] CCFE, United Kingdom Atomic Energy Authority, Abingdon, Oxfordshire OX14 3DB, United Kingdom

*Corresponding authors:
Email addresses: B. Cai: b.cai@bham.ac.uk D. Nguyen: Duc.Nguyen@ukaea.uk

Abstract

We investigated the mechanical and microstructural responses of a high-strength equal-molar medium entropy FeCrNi alloy at 293 and 15 K by *in situ* neutron diffraction testing. At 293 K, the alloy had a very high yield strength of 651 ± 12 MPa, with a total elongation of $48 \pm 5\%$. At 15 K, the yield strength increased to 1092 ± 22 MPa, but the total elongation dropped to $18 \pm 1\%$. Via analyzing the neutron diffraction data, we determined the lattice strain evolution, single-crystal elastic constants, stacking fault probability, and estimated stacking fault energy of the alloy at both temperatures, which are critical parameters to feed into and compare against our first-principles calculations and dislocation-based slip system modeling. The density functional theory calculations show that the alloy tends to form short-range order at room temperatures. However, atom probe tomography and atomic-resolution transmission electron microscopy did not clearly identify the short-range order. Additionally, at 293 K, experimental measured single-crystal elastic constants do not agree with those determined by first-principles calculations with short-range order, but agree well with the values from the calculation with the disordered configuration at 2000 K. This suggests that the alloy is at a metastable state resulted from the fabrication methods. In view of the high yield strength of the alloy, we calculated the strengthening contribution to the yield strength from grain boundaries, dislocations, and lattice distortion. The lattice distortion contribution was based on the Varenne-Luque-Curtine strengthening theory for multi-component alloys, which was found to be 316 MPa at 293 K and increased to 629 MPa at 15 K, making a significant contribution to the high yield strength. Regarding plastic deformation, dislocation movement and multiplication were found to be the dominant hardening mechanism at both temperatures, whereas twinning and phase transformation were not prevalent. This is mainly due to the high stacking fault energy of the alloy as estimated to be 63 mJm^{-2} at 293 K and 47 mJm^{-2} at 15 K. This work highlights the significance of lattice distortion and dislocations played in this alloy, providing insights into the design of new multi-component alloys with superb mechanical performance for cryogenic applications.

Keywords
medium entropy alloy, multi-component alloy, cryogenic temperature, neutron diffraction

1. Introduction

In the past decade, a revolutionary new metallurgy design strategy, multi-component alloys (MCAs), containing several equimolar or non-equimolar components (in the range of 5-35 at.%), has been developed [1], which include high entropy alloys (HEAs) and medium entropy alloys (MEAs). Among different groups of MCAs, the group based on $3d$ transition elements (Cr, Mn, Fe, Co, Ni, V, and Cu) can form a single face-centered cubic (FCC) structure, which shows great potential in achieving superior strength-ductility combinations [2–9]. The compositions include FeNiCo MEA [2], FeMnCoCr HEA [8], CrMnFeCoNi HEA [9], and other variations.

Recently, the intriguing mechanical performance of $3d$ element-metal MCAs under cryogenic temperatures has been demonstrated, such as high fracture tolerance [9], fatigue-crack growth resistance [10], and exceptional strength-ductility balance [11,12]. This makes them highly desirable in the rapid-growing cryogenic applications such as liquid gas storage, fusion reactors, and medical diagnosis. The application of MCAs at cryogenic temperatures, however, can be severely limited since the yield strength (YS) of those alloys is relatively low compared to conventional structural alloys. Many studies show the YS of these MCAs is generally lower than 400 MPa at room temperature and 500 MPa at cryogenic temperatures [2,13]. For example, the YS of a single-phase FeCoCrNi HEA is only 260 MPa at 293 K and 480 MPa at 77 K [13]. Therefore, several conventional strengthening strategies (such as precipitating hardening and grain refinement) were applied to overcome this dilemma via introducing extensive dislocations and interfaces.

Based on the uniqueness of MCAs, two promising strengthening strategies are emerging to resolve this dilemma: chemical short-range order (SRO) [14–16] and severe lattice distortion (i.e., a wide fluctuation of the atomic bond distances) [1]. SRO stems from the enthalpic interactions among constituent elements, and its formation is thermodynamically favored in MCAs [14–16]. The densely distributed SROs can create strain fields; thus, an extra force is required to break the SROs when dislocations pass by. The cutting-through and the following de-trapping process during dislocation migration are expected to increase the opportunity for dislocation to interact and form entanglement [15]. SROs have been observed in a VCoNi [14] and a long-time-annealed CrCoNi alloy [16].

Severe lattice distortion originates from the randomly distributed constituent elements with varying atomic radii as no matrix or host element could be defined in MCAs [1]. Each individual atom in MCAs thus experiences different stress fields created by its interaction with a set of different neighboring atoms. The role of the severe lattice distortion in strengthening the MCAs is under debate. Wu et al. [17] suggested that the large lattice distortion fluctuation can only provide weak Labusch-type pinning effects on dislocation motions. However, research has shown that enhancing the lattice distortion by adding extra vanadium can induce a significant YS improvement in both FCC and body-centered cubic (BCC) HEAs [4]. The critical role of lattice distortion in strengthening was also confirmed by theoretical studies, which successfully predicted the YS of several MCAs using solute misfit volumes as the core parameter [18,19]. These theories also predicted the growing strengthening effect of lattice distortion with decreasing temperature [2].

2

Herein, we studied a new equimolar ternary MEA (FeCrNi alloy), which has been shown to achieve a high YS (644MPa) and good elongation (54%) at room temperature [20]. Several critical questions can be raised for this alloy: (i) Does SRO exist in the FeCrNi alloy, as observed in CrCoNi [15] and VCoNi MEAs [14]? Is SRO the main strengthening factor? (ii) To what degree the severe lattice distortion can strengthen the alloy and what is its strengthening contribution at cryogenic temperatures? In addition, the alloy should have high stacking fault energy >50 mJm^{-2} according to Ref. [21]. Twinning and phase transformation should not be operative, but the alloy still has very good ductility, so what are the underpinning mechanisms for the alloy to have a balanced combination of strength and ductility? This study intends to provide insights into these questions.

2. Materials and Methods
2.1 Materials

Powder metallurgy was used to produce the FeCrNi MEA with a nominal composition of $Fe_{33.3}Cr_{33.3}Ni_{33.3}$. Detailed procedures for the fabrication can be found in [20]. High purity (>99.99%) Fe, Cr, and Ni raw materials were melted in an induction vacuum furnace. The melted liquid was dropped through a ceramic cube and atomized by high purity Ar with a pressure of 4 MPa. The formed powder, with an average diameter of 50 μm, was then capsulated in a steel cylinder chamber (Φ50 × 150 mm). After degassing and preheating to 1200 °C for 1 h, the sample was subjected to hot extrusion immediately with an extrusion ratio of 7:1 and a velocity of ~10 mm/s. The extruded bars were then cooled down to room temperature in the air. Samples for tensile tests were machined along the extrusion direction. The actual chemical composition of the sample was measured to be $Fe_{33.7}Cr_{33.7}Ni_{32.5}$ (at. %) by inductively coupled plasma mass spectrometry (ICP-MS).

2.2 *In situ* neutron diffraction

In situ time of flight neutron diffraction measurements during tensile tests were carried out at the beamline of ENGIN-X at ISIS, spallation neutron source, the Rutherford Appleton Laboratory, UK. The schematic illustration of the time-of-flight neutron diffractometers and strain scanner can be seen in our previous work [22]. Originally, a pulsed beam of neutrons with a wide energy range (incident beam) traveled through a 100 K liquid methane moderator, and its horizontal and vertical angular divergence was then modified by two pairs of motorized slits (4 × 4 mm^2). A vacuum chamber and a 50 kN hydraulic stress rig with a horizontal loading direction (LD) were mounted 45° to the incident beam. Behind the collimators (4 mm wide), two diffraction detector banks (radial and axial) were centered on a horizontal diffraction angle of ±90° to the incident beam to collect the diffraction signals from grain planes subjected to tensile and compressive load, respectively. Before the tests, instrument parameters (e.g., primary and secondary flight path distances) and instrumental peak broadening effects were determined by measuring a strain-free standard CeO_2 calibrant. Dog-bone tensile samples were mounted on the stress rig then the high vacuum and low-temperature conditions were stabilized for half an hour before the test. Diffraction patterns were collected for 20-min intervals between each loading step, iterating until fracture. Stress-control and displacement control were used at the elastic and plastic stages, respectively. The *in situ* neutron diffraction and tensile testing were repeated on two specimens for both temperatures. The data collected at the same

condition is very similar, and thus, the reproducibility was confirmed and only one of the data was analyzed. Rietveld refinement and single peak fitting (with pseudo-Voigt function) were performed with the GSAS software, allowing the determination of lattice parameters, peak position, and full width at half maximum (FWHM) of the peaks. The lattice strain is defined as the change of inter-planar spacing with respect to its original inter-planar spacing. Its evolution can be calculated by [3]:

$$\varepsilon_{hkl} = \frac{d_{hkl} - d_{hkl}^0}{d_{hkl}^0},$$

(1)

where ε_{hkl} is the lattice strain of $\{hkl\}$ grain family, d_{hkl} and d_{hkl}^0 is corresponding lattice spacing at the current stress state and stress-free state, respectively. Procedures for single crystal constant and dislocation density calculations were included in the Supplementary Materials.

2.3 First principal calculation

Density Functional Theory (DFT) for elastic constant calculations were performed within the Vienna Ab-initio Simulation Package (VASP) using the Projector Augmented Wave (PAW) method and spin-polarized electronic structure scheme [23,24]. The electron exchange-correlation functional was in the Generalized Gradient Approximation (GGA) treated with Perdew-Burke-Ernzerhof parametrization [25]. All the calculations in this work were carried out within the PAW potentials for Cr, Fe, and Ni without semi-core electrons with the core configurations $[Ar]3d^4s^1$, $[Ar]3d^7s^{1,}$ and $[Ar]3d^9s^1$, respectively. The plane wave cut-off energy for the most of calculations was 400 eV. The total energy was converged to 10^{-6} eV/cell and the force components were relaxed to 10^{-3} eV/Å. Total energies used for elastic constant calculations were performed using the Monkhorst-Pack meshes [26] with $4 \times 4 \times 4$ k-point for both $3 \times 3 \times 3$ FCC-supercell configurations with 108 atoms per unit cell configurations and additional calculations with the $6 \times 6 \times 6$ k-point meshes were also performed for checking the convergence. A more detailed description of elastic constants from first-principles DFT calculations in different intermetallic phases can be found in Refs. [27–32].

For disordered alloys, conventional approaches for evaluating elastic constants from DFT techniques are usually based on so-called Coherent Potential Approximation (CPA) from which a single site mean field theory is applied to treat completely random configurations with different chemical compositions. The CPA method has been employed to investigate elastic property maps from DFT calculations for the case of concentrated random FCC Fe-Cr-Ni alloys which are the main base for austenitic stainless steels [33,34]. In the present study, an alternative DFT approach was employed to study the elastic properties of the FeCrNi medium-range entropy alloys. It was based on our recent and systematic work on the phase stability of both FCC and body-centered-cubic (BCC) Fe-Cr-Ni magnetic alloys using a combination of first-principles constructed Cluster Expansion (CE) Hamiltonian with exchange Monte-Carlo (MC) simulations at a finite temperature [35].

The new approach allows us to investigate not only the free energy but also the disorder-order transition of alloys as a function of composition and temperature in terms of Warren-Colley [36,37] SRO effects between different pairs of atoms. The theoretical expression of SRO parameters has recently been derived for MCAs in a matrix formulation [38–41]. The

chemical SRO parameter $\alpha_n^{A,B}$ between two species A and B for the n-th nearest neighbor shell can be defined as follows:

$$\alpha_n^{A,B} = 1 - \frac{y_n^{A,B}}{x_A x_B},$$

(2)

where $y_n^{A,B}$ denotes the pair probability, x_A and x_B are the concentration of A and B atoms, respectively. Segregation between A and B components gives rise to positive $\alpha_n^{A,B}$, whereas the negative value of $\alpha_n^{A,B}$ means that there is a chemical ordering between them. When $\alpha_n^{A,B} = 0$, A and B atoms are found to be randomly distributed in alloys. Fig. 1a and 1b show the atomistic configurations of medium-range and equiatomic FeCrNi alloys obtained from the present MC simulations of the 9 × 9× 9 FCC supercell for the two temperatures: 300 K (Fig. 1a) and 2000 K (Fig. 1b), respectively.

For the practical study of elastic constants in the FeCrNi system from first-principles methods, it is more convenient to reduce the supercell size 9 × 9 × 9 (Fig. 1a and 1b) to 3 × 3 × 3 (Fig. 1c and 1d) in order to balance between computational time and accuracy of DFT calculations. Furthermore, for the high-temperature disordered configurations, the symmetry of the supercell is very low (space group *P1*) due to the random distribution of atoms in the supercell. Here, for obtaining the individual components of the elastic constants matrix, we applied the method based on the deformation of an unstrained structure and the analysis of the changes in the total energy, E_{tot}, computed using DFT as a function of strain [42–45]. The deformation leads to a change in the total energy of the crystal according to the following expressions:

$$U = \frac{E_{tot} - E_0}{V_0} = \frac{1}{2} \sum_{i=1}^{6} \sum_{j=1}^{6} c_{ij} \varepsilon_i \varepsilon_j,$$

(3)

where E_0 is the total energy of the unstrained lattice, V_0 is the volume of the undistorted cell and the C_{ij} are the elements of the elastic constant matrix with a notation that follows standard convention. Both i and j run from 1…6 in the sequence $\{xx, yy, zz, yz, xz, xy\}$. For each considered deformation, 8 magnitudes of strain (±0.2%, ±0.4%, ±0.6%, ±0.8%) were applied. The dependencies of the total energy on the deformation were then fitted to quadratic equations and the respective elastic constants were obtained.

To study the elastic properties of Fe-Cr-Ni alloys at high-temperature configuration (T=2000 K), strains were applied for 9 different deformation modes:

$$\varepsilon_1 = \{xx, 0,0,0,0,0\}$$

$$\varepsilon_2 = \{0, yy, 0,0,0,0\}$$

$$\varepsilon_3 = \{0,0, zz, 0,0,0\}$$

$$\varepsilon_4 = \{xx, yy, 0,0,0,0\}$$

$$\varepsilon_5 = \{xx, 0, zz, 0,0,0\}$$

$$\varepsilon_6 = \{0, yy, zz, 0,0,0\}$$

$$\varepsilon_7 = \{0,0,0, yz, 0,0\}$$

$$\varepsilon_8 = \{0,0,0,0, xz, 0\}$$

$$\varepsilon_9 = \{0,0,0,0,0, xy\}$$

This allowed obtaining 9 elements of the elastic constant matrix:

$$(C_{ij}) = \begin{bmatrix} C_{11} & C_{12} & C_{13} & 0 & 0 & 0 \\ C_{12} & C_{22} & C_{23} & 0 & 0 & 0 \\ C_{13} & C_{23} & C_{33} & 0 & 0 & 0 \\ 0 & 0 & 0 & C_{44} & 0 & 0 \\ 0 & 0 & 0 & 0 & C_{55} & 0 \\ 0 & 0 & 0 & 0 & 0 & C_{66} \end{bmatrix}. \tag{4}$$

Note: In this study, we assumed that the elements of the elastic constant matrix other than C_{11}, C_{12}, C_{13}, C_{22}, C_{23}, C_{33}, C_{44}, C_{55}, C_{66} are equal to zero. Based on our previous study with structures with low symmetry [45], the values of those elements are usually much smaller than C_{11}, C_{12}, C_{13}, C_{22}, C_{23}, C_{33}, C_{44}, C_{55}, C_{66} and can therefore be neglected. Therefore, the lack of those constants should not significantly influence the predictions of the overall elastic properties of alloys. For the low-temperature configuration (T=300 K), the elastic tensor matrix elements (4) have been computed by direct diagonalization following the tetragonal symmetry as it will be discussed in the Modelling section.

Afterward, we applied the calculation method of the anisotropy of Young's modulus and Poisson's ratio proposed by Wróbel et al. [32] to investigate the anisotropy of elastic properties. In order to obtain the theoretical values of elastic moduli for polycrystalline materials, the Reuss-Voigt-Hill method has been employed [46]. The detailed procedure can be found in Section 4 of the Supplementary Materials.

2.4 Microstructure characterization

The microstructure characterizations were performed on the samples sectioned from the fractured tensile bars using electrical discharge machining. The samples were metallographically polished before electron backscatter diffraction (EBSD) test on an HKL EBSD detector based on a scanning electron microscope (SEM, TESCAN MIRA 3, Czech Republic). The SEM parameters for the EBSD were set to a voltage of 20 kV, a current of 25 nA, and a step size of 1.5 μm. The EBSD data analysis was carried out with HKL Channel 5 software. To avoid ambiguous grain boundaries, misorientation angles less than 2° were ignored during the analysis. The thin foils for scanning transmission electron microscope (STEM) observation were mechanically polished to a thickness of ~80 μm

before the twin-jet electropolishing using a constant current of 150 mA in a solution of 5% perchloric acid and 95% methanol cooled to -30 °C. The bright-field TEM observation was undertaken on a Tecnai G^2 F30 microscope operated at 300 kV. The atomic-resolution high-angle annular dark-filed STEM (HAADF-STEM) images were performed on an aberration-corrected Titan 60-300 microscope at a voltage of 300 kV. The collection half-angle of the HAADF detector ranging from 60 to 290 mrad was used, with the convergence half-angle of 21.4 mrad, giving a probe size of ~1.2 Å. The dilatation field of the lattice was analyzed with the geometric phase analysis (GPA) method on the software Strain++ [47], during which a dislocation-free region was chosen as a reference.

Needle-shaped samples for atomic probe tomography (APT) were prepared by lift-out and annular milled in an FEI Scios focused ion beam (FIB)/SEM. The APT characterizations were performed in a local electrode atom probe (CAMEACA LEAP 5000 XR). The specimens were analyzed at 70 K in voltage mode, at a pulse repetition rate of 200 kHz, a pulse fraction of 20%, and an evaporation detection rate of 0.3% atom per pulse. The 3D reconstructions and data analysis were performed on Imago Visualization and Analysis Software (IVAS) version 3.8.

3. Experimental results
In this section, we first presented the microstructure and mechanical performance of the alloy at 293 and 15 K. We then presented the analysis of the *in situ* neutron diffraction spectra including the lattice strain, single-crystal elastic constants, the evolution of stacking fault probability (SFP) and dislocation density. Post-mortem TEM characterization was presented afterward.

3.1 Initial microstructure

Fig. 2 shows the micro to nanoscale microstructure of the virgin FeNiCr alloy characterized by SEM-based BSE, EDS, EBSD, HRTEM, and APT. According to the EBSD inverse pole figure (IPF) map on the plane perpendicular to the loading direction (Fig. 2a), the alloy is composed of large equiaxed grains with annealing twins. The average grain size of ~23.4 μm was determined by performing the line-intercept method on the EBSD maps excluding the annealing twin boundaries. In Fig. 2b, the band contrast map was overlapped with the boundaries map of Fig. 2a. The low-angle grain boundaries (LAGBs) were defined as misorientations with $15° \geqslant \theta \geqslant 2°$ (shown in red lines) while the high-angle grain boundaries (HAGBs) comprise misorientations larger than 15° (shown in black lines). The annealing twin boundaries (TBs) were defined as $\Sigma3=60°\{111\}$ (shown in blue lines). The fraction of LAGBs is very low (less than 2%) and most of the boundaries were HAGBs. In addition to grain boundaries, a large fraction of annealing TBs was observed. SEM-BSE and corresponding EDS analysis results (Fig. 2c) show a small amount of Cr-rich phase located at grain boundaries. Typical bright-field TEM images of the annealing twin structure are shown in Fig. 2d. Two straight and parallel twin boundaries can be identified with a spacing distance of ~2.18 μm. The twin relationship is confirmed by the corresponding selected area diffraction (SAED) pattern inserted in Fig. 2d.

The chemical homogeneity of the alloy matrix was confirmed by APT analysis at the atomic scale. Fig. 2e displays the three-dimensional (3D) elemental maps of the three constituent elements, Fe, Cr, and Ni, from a reconstructed volume of $50 \times 50 \times 140$ nm^3

containing ~12 million ions. There is no apparent elemental segregation in the tested volume. The tested region was found to have a composition of Fe 34.7, Ni 31.8, and Cr 33.5 (at.%), showing an acceptable match to the bulk composition obtained from the ICP-MS. Furthermore, the homogeneity of the atomic distribution of the alloy was also evaluated with the chi-squared statistics with a frequency distribution analysis (FDA) shown in Fig. 2f. The curves from the binomial simulation match well with the curves obtained from the experiments, indicating a randomly distributed solid solution. The parameters used for qualifying the fit are shown in the insert table in Fig. 2f. The normalized homogenization parameter, μ, for all three constituent elements are very close to 0, confirming their random distribution.

As reported in Refs. [15,16], the existence of SROs can be confirmed by the diffuse superlattice features in the HRTEM images and the streaking intensity along the reciprocal lattice vectors in corresponding FFT images. Therefore, to determine if SROs exist in the present alloy, we took over 20 HRSTEM images along different zone axes on the undeformed sample. Two of them are shown in Fig. 2g and 2h, the inset images are the corresponding two-dimensional fast Fourier transforms (FFT) of the HRTEM images. Very vague diffusion disks were observed only in one of the HRTEM images (Fig. 2h), which may indicate the formation of a trace amount of SRO in the present alloy.

3.2 Tensile properties

Fig. 3a shows the engineering and true stress-strain curves (up to the UTS points) of the FeCrNi alloy at 293 and 15 K. The alloy shows a high YS of 651 ± 12 MPa and UTS of 1020 ± 3 MPa, as well as a great elongation of $48 \pm 5\%$ at 293 K. The mechanical properties of the alloy, were then compared with other high strength steels and single or multiphase MEAs/HEAs as shown in Fig. 3b, in which the YS was plotted with respect to total elongation [2,3,54,55,8,10,48–53]. The FeCrNi alloy shows an advantage in achieving high YS and a large elongation combination compared to other MCAs at 293 K.

At 15 K, the YS of the FeCrNi alloy increased to 1092 ± 27 MPa, the UTS increased to 1451 ± 2 MPa, while the total elongation decreased to $18 \pm 1\%$. Corresponding values of strength and ductility are listed in Table 1. We have also listed the mechanical properties of several HEA/MEA and FCC alloys at 15 K or lower in Table 1. The YS of FeCrNi alloy is highest among the listed alloys, although its elongation is much lower.

Table 1 Uniaxial tensile properties of different alloys at 293 K and cryogenic temperature

Alloy	Temperature [K]	YS [MPa]	UTS [MPa]	Elongation [%]
FeCrNi	293	651 ± 12	1020 ± 3	48±5
FeCrNi	15	1092 ± 22	1451 ± 2	18±1
FeCoCrNiMo $_{0.2}$ [11]	15	710	1423	42
CrMnFeCoNi [12]	15	740	2500	62
CrCoNi [56]	15	670	2292	60
316LN stainless steel [57]	4.2	1045	1528	33

3.2 Neutron diffraction spectra

The *in situ* neutron diffraction patterns during tensile testing at 293 and 15 K plotted with respect to true stress were shown in Fig. 4a and 4b, respectively. Five reflections of {111}, {200}, {220}, {311}, and {222} from the single FCC phase can be observed at both 293 and 15 K before deformation. During and after the tensile testing at both temperatures, no new peaks appeared, indicating the FCC structure was stable and maintained as a single FCC phase solid solution under loading. The lattice parameter (a_0) was obtained by performing Rietveld refinement on neutron diffraction patterns. The lattice parameter decreased slightly from 3.602 to 3.594 Å as the temperature decreased from 293 to 15 K due to the shrinkage of atomic bands [22].

The measured lattice strain from five crystallographic planes of ({111}, {200}, {220}, {311}, and {222}) along axial and radial direction were plotted as a function of true stress in Fig. 5a (293 K) and 5b (15 K). The uncertainties in the measured internal strains were approximately 30 microstrain. The measured bulk elastic Young's modulus (E_M) at different temperatures were obtained by linear fitting the true stress and strain curves at the elastic stage. Similarly, the elastic constants of each orientation (E_{111}, E_{200}, E_{220}, and E_{311}) were then obtained by linear fitting the lattice strain and true stress before yielding (Table 2). After yielding, the orientation-dependent yielding behaviors were observed at both temperatures. As indicated in Fig. 5a and 5b, the {111} grain family has the highest stiffness (E_{111} of 248.1 GPa at 293 K and 260.4 GPa at 15 K). It, however, showed the earliest yielding behavior (~550 MPa at 293 K and ~1000 MPa at 15 K). Meanwhile, among all 4 grain families, {200} showed the lowest stiffness (E_{200} of 148.6 GPa at 293 K and 162.3 GPa at 15 K) and a delayed yielding behavior (~730 MPa at 293 K and ~1150 MPa at 15 K). The varied stiffness and yielding behaviors among different grain families can be ascribed to the elastic and plastic anisotropy of the crystals. After yielding of some stiff grain families (e.g. {111}), the external stress gradually transferred to other soft grain families (e.g. {200}).

Table 2 Experimentally measured elastic properties of the FeCrNi alloy at different temperatures

Temp. [K]	E [GPa]	E_{111} [GPa]	E_{200} [GPa]	E_{220} [GPa]	E_{311} [GPa]	v_{111}	v_{200}	v_{220}	v_{311}	v	G [GPa]
293	200.5	248.1	148.6	220.7	185.9	0.256	0.339	0.314	0.335	0.292	77.6
15	237.2	260.4	162.3	225.7	197.2	0.233	0.320	0.282	0.302	0.281	92.6

3.3 Single-crystal elastic constants calculation

During elastic deformation, the lattice parameter obtained at axial and radial directions increased linearly with true stress. Their slopes at radial and axial directions were obtained by linear fitting and the ratio of the two slopes determines the Poisson's ratio (v). Then the shear modulus (G) was obtained via $G = E/2(1 + v)$. The drop of deformation temperature increased the stiffness of the alloy as the E_{hkl} at all four orientations increased to varying degrees.

To better understand the underlying elastic deformation behavior of the alloy at different temperatures, several materials properties, including macroscopic elastic, shear, and bulk moduli (E_M, G_M, and K_M), were calculated from diffraction elastic moduli (E_{hkl}) and

Poisson's ratio (v_{hkl}) using the Voigt, Reuss, and Kroner models [58]. The detailed procedure can be found in Section 1 of the Supplementary Materials. In Fig. 6a and 6b, the two reciprocal diffraction elastic constants ($1/E_{hkl}$ and v_{hkl}/E_{hkl}) obtained from experimental elastic lattice strain and calculated with Voigt, Reuss, and Kroner models are plotted with respect to the elastic anisotropy factor ($A_{hkl} = \frac{h^2k^2+h^2l^2+k^2l^2}{(h^2+k^2+l^2)^2}$) at 293 and 15 K, respectively. The fitting results indicate that among all three models, the Kroner model shows the best agreement with the experimental results at both 293 and 15 K. The Voigt model simply assumes that all grains were uniformly strained, but the force among grains cannot meet the equilibrium. While in the Reuss model, homogeneous stress was assumed to be applied to all grains, but the distorted grains cannot fit together. Therefore, due to their simplicity, the Voigt and Reuss model are generally used to define the upper and lower bounds of the diffraction and isotropic macroscopic elastic constants. By contrast, the Kroner model provides a more accurate estimation of elastic properties after considering the orientation dependence of elastic parameters. The single-crystal elastic constants, elastic, polycrystalline moduli, and Poisson's ratio at 293 and 15 K calculated by this method are listed in Table 4. The values of C_{11} and C_{44} decreased slightly as the temperature decreased from 293 to 15 K, while C_{12} remains nearly constant.

The orientation-dependent elastic properties of the FeNiCr alloy at 293 K (determined from neutron diffraction and DFT simulation results) were illustrated in Fig. 7. To calculate the elastic properties in any direction, the fourth-order elastic tensor was transformed in a new basis with Eq. (S20) in the Supplementary Materials. The experimentally determined elastic properties of the alloy were illustrated with the three-dimensional (3D) surfaces (left column). The experimental results along directions at XY, XZ, and YZ planes were shown in the middle column by 2D contours. Young's modulus is shown in Fig. 7a and 7e. The maximum and minimum values of 302 and 119 GPa were observed at <111> and <100> direction, respectively. The ratio of maximum-to-minimum elastic modulus of 2.5 indicates the high anisotropy property of the alloy. The 3D surfaces of shear modulus and Poisson's ratio were shown in Fig. 7b and 7f, respectively. The translucent outer surface represents the maximum value while the solid surface inside shows the minimum values. The maximum and minimum values were shown with dashed and solid lines in the corresponding 2D contours. The maximum value of the shear modulus (127 GPa) appeared at <100> direction whereas the minimum value of 55.3 GPa is in <110> direction, yielding the ratio of the maximum to the minimum shear modulus of 2.3 (Fig. 7c and 7g). For Poisson's ratio, the maximum value of 0.4 (<100> direction) while the minimum value is approaching 0 (Fig. 7c and 7g). In Fig. 7d and 7h, the linear compressibility (LC) has a value of 1.9 TPa^{-1}, showing negligible anisotropy in all directions.

3.4 Stacking fault probability

The SFP measures the amount of stacking faults formed during deformation and allows the determination of the stacking fault energy (SFE) [11,13] of the alloy. The detailed procedure of SFP and SFE calculations can be found in Section 2 of the Supplementary Materials. The measured SFP evolution of the FeNiCr alloy at 293 K and 15 K is compared with another HEA (FeCoCrNiMo$_{0.2}$) (Fig. 8a) [3]. At high strain levels, the FeCoCrNiMo$_{0.2}$ showed a very high level of SFP. It can reach 2.9×10^{-2} at 77 K and even increase to $5.1 \times$

10^{-2} at 15 K. The alloy has a very low SFE of 17 mJm^{-2} and 11 mJm^{-2} at 77 and 15 K, respectively. By contrast, the SFP of FeNiCr alloy is very low (below 7×10^{-3}) at both temperatures. According to Eq. (S13), the SFE of the alloy was estimated to be 63 ± 4 mJm^{-2} at 293 K and 47 ± 3 mJm^{-2} at 15 K.

Generally, the SFE of an alloy serves as one of the most crucial parameters determining the dominant deformation mechanisms. The strain hardening effects were mainly controlled by dislocation motion when the SFE exceeds 45 mJm^{-2}. As the SFE decreased to the range of 18~45 mJm^{-2}, twinning is preferable to occur. While phase transformation, from the parent FCC to newborn phases with hexagonal close-packed (HCP) and/or body-centered tetragonal (BCT) structures may occur if the SFE is further decreased to be lower than 18 mJm^{-2} [11,22,59]. The thermodynamic calculation results indicate that the SFE of the FeNiCr alloy is in the range of 50~60 mJm^{-2} [59]. This is also confirmed in Refs. [5,21], where the high SFE of the FeNiCr was predicted to be >50 mJm^{-2} by large-scale atomic simulations. These previous studies agree with our calculation based on the diffraction data analysis. The high SFE of the FeNiCr alloy (63 ± 4 mJm^{-2} at 293 K and 47 ± 3 mJm^{-2} 15 K) suggests that its deformation behavior is mainly controlled by the dislocation motion, while the stacking fault, twins, and phase transformation are less likely to operate during deformation. This also means that the alloys are kept as non-magnetic during deformation at very low temperatures, which is favorable for applications in super-strong magnets.

The high SFE of the FeNiCr alloy can be attributed to two reasons: (1) the low configurational entropy and (2) the high concentration of Cr and Ni. Zaddach et al. [5] applied diffraction methods and first-principles calculations to investigate the SFE of a series of MCAs (FeCoNiCrMn) and the results indicated that the SFE decreases with the increase of element complexity, i.e., constituent number or configurational entropy. On the other hand, Ref. [60] indicates that the SFE of an alloy is the combined effect of each constituent element. The same element can influence the SFE differently in different alloy systems. For the FeCoNiCrMn alloy system, the SFE can be increased by increasing Ni contents due to the high intrinsic SFE of Ni (~125 mJm^{-2}) [61]. This also agrees with the study of Bonny et al.[21], which suggests that the SFE of FeNiCr alloy can be significantly increased by increasing Cr and Ni contents.

3.5 Dislocation density evolution

The dislocation density evolution of the alloy during deformation was calculated with the modified Williamson-Hall method [62]. The detailed procedure for dislocation density calculation can be seen in Section 3 of the Supplementary Materials. The calculated dislocation density against true strain at both temperatures is shown in Fig. 8b. The evolution of dislocation density showed a very similar pattern at both temperatures. The dislocation density fluctuated slightly at around 6×10^{13} m^{-2} before yielding, after which both curves increase almost linearly upon further straining. At 293 K, the dislocation density of 1.74×10^{15} m^{-2} was achieved at true stress of 1392 MPa and a true strain of 0.31. At 15 K the dislocation density reached 7.93×10^{14} m^{-2} at true stress of 1576 MPa and a true strain of 0.12.

Meanwhile, the dislocation evolution is closely related to the texture development during tensile loading. The intensity of each reflection (<111>, <200>, <220>, <311>, and <222>) was normalized with that of the stress-free state and their evolution with true stress at 293

and 15 K are shown in Fig. 8c and 8d, respectively. At both temperatures, the peak intensity curves changed very little during the elastic stage while they started to vary after the yielding points. This originates from the difference in grain rotation in response to external loading. At 293 K, after yielding, (111)//LD and (222)//LD oriented grains gradually rotated towards the loading direction, making their peak intensity increase almost linearly with the increase of true stress during subsequent straining. By contrast, the intensity of (200) peak maintained at a similar level of ~0.8 after a slight dropping. The intensity of the other two peaks, (311) and (220), decreased to 0.43 and 0.09, respectively, as grains with these orientations gradually rotated away from LD. A similar phenomenon was also observed at 15 K (Fig. 8b) and reported in Refs. [3,13]. In the present study, the (111)//LD texture was used as a measure of the dislocation activity as the texture development is characteristic of dislocation slip during plastic deformation [12]. The highest (111) intensity reached 2.62 at 293 K, compared with a much lower value of 1.29 at 15 K. Meanwhile, at 293 K the texture developed at a faster pace (with a slope of ~2.35×10^{-3} MPa^{-1}) than that at 15 K (with a slope of ~0.67×10^{-3} MPa^{-1}). The slow texture change at 15 K also explains the lower strength enhancement after yielding and deterioration of the ductility observed at 15 K (Fig. 3). The inactive grain rotation and slow texture evolution limited the dislocation motions to well-oriented grains and led to the inability of catering to larger external strain [63]. Meanwhile, fewer slip systems can be activated in those "not-so-good-oriented" grains, leading to a much lower dislocation density achieved at 15 K. This result is in good agreement with the mechanical performance (Fig. 3a) and the dislocation density evolution (Fig. 8b).

3.6 TEM characterization of the strained samples

To further reveal the underlying deformation mechanisms, post-mortem TEM characterizations were performed on the fractured samples deformed at 293 and 15 K. The bright-field TEM images were taken at a two-beam condition while the SAED patterns of the corresponding area were collected along <110> zone axis and attached to the image. Fig. 9a shows the bright-field STEM micrograph of the alloy deformed to a low strain level of ~0.1 at 293 K. Massive parallel shear bands traveling through the whole grain interior were observed. The image on the inset of Fig. 9a is the SAED pattern taken from the area highlighted by the yellow circle, showing the matrix still maintained an FCC structure. The shear bands mainly consisted of closely arrayed dislocation walls whereas no SFs or twins were detected, indicating the alloy deformed by typical planar dislocation glide on {111} planes. The shear bands were magnified in Fig. 9b, showing that the dislocation walls consisted of massive dense parallel primary {111} slip traces. Fig. 9c is the bright-field TEM image taken from the sample sectioned near the fracture surface. Dense dislocation networks were produced between slip traces. Secondary {111} slip occurred and intersected with the primary slip traces, separating the matrix into small parallelogram blocks. No SFs or twins were formed according to the corresponding SAED patterns. The mean free path of mobile dislocations can be effectively reduced by the concentrated slip bands.

Similar dislocation motions were also observed at 15 K. Fig. 9d is the bright-field TEM image and corresponding SAED pattern showing the microstructure of the alloy deformed to a strain of ~0.1 at 15 K. Comparing with Fig. 9b, the secondary slip system is more easily activated at 15 K, and more dislocation tangling kinks were observed. Dislocations

were preferably gathered around the crossing slip systems and formed parallelogram blocks. The interior of the nanosized dislocation substructure shows a relatively lower dislocation density than the block boundaries. The morphologies of dislocation networks deformed to a strain of ~0.1 and near the fracture surface were further revealed by STEM-HAADF images in Fig. 9e and 9f, respectively. The while lines were identified as dislocation traces according to the HRTEM image (Fig. 9f). In Fig. 9f, the density of intersecting active slip planes increased significantly as more slip systems were activated, refining the spacing between coplanar slip bands significantly. The concentrated slip bands can hinder dislocation slip on parallel slip bands by increasing the passing stresses. Furthermore, rapid dislocation multiplication occurred in both dislocation walls and the small dislocation-free zones (Fig. 9e), thickening the dislocation walls effectively and gradually expanding dislocations to the whole block interior (Fig. 9f). Fig. 9g displays the HAADF image of a slip trace junction in Fig. 9f. Fig. 9h is the lattice dilatation resulting from the presence of a high strain field, obtained from the trace of the lattice distortion matrix via the GPA method [47]. This result identified the crossing slip traces, especially their junctions, mainly consisted of tangling dense dislocations accompanied by a high residual strain field. It is also worth noting that at both temperatures, very few short and isolated stacking faults were observed from our STEM observation, which is consistent with our neutron diffraction results in Fig. 8a.

4 Modelling results

In this section, we used density functional theory calculation to identify SRO and determine the single-crystal elastic constants, which were compared against experimental results. Via dislocation-based slip system modeling with key parameters taken from the neutron diffraction data, we were able to determine strengthening sources contributing to the yield strength, and the underlying factors controlling strain hardening during plastic deformation for the FeCrNi alloy.

4.1 Phase formation parameters

Several thermodynamic parameters related to phase formation including ΔS_{mix} (entropy of mixing), ΔH_{mix} (enthalpy of mixing), and T_m (melting point) were calculated (see Section 5 of the Supplementary Materials). Besides, the parameter Ω, which can be applied to predict the solid-solution formation of random MCAs was calculated according to Ref. [64]:

$$\Omega = \frac{T_m \Delta S_{mix}}{|\Delta H_{mix}|}. \tag{5}$$

When $\Omega > 1$, the MCAs are mainly composed of solid solutions while $\Omega \leqslant 1$, the formation of intermetallic compounds or segregations are favored.

Another important parameter in predicting the solid-solution formation is the parameter δ [64], which describes the atomic size difference of the MCAs and can be expressed as follows:

$$\delta = \sqrt{\sum_{i=1}^{n} c_i (1 - \frac{r_i}{\bar{r}})^2}, \tag{6}$$

, where r_i is the atomic radius and $\bar{r} = \sum_{i=1}^{n} c_i r_i$ is the average atomic radius. According to Refs. [64,65], when $\Omega \geq 1.1$ and $\delta \leq 6.6\%$, stable solid-solution phases can be formed in MCAs.

Furthermore, Guo et al. [66] indicated that the valence electron concentration (VEC) serves as a criterion for determining the lattice structure of the MCAs as it correlated a structure's VEC with its FCC/BCC phase formation. It is defined by:

$$VEC = \sum_{i=1}^{n} c_i (VEC)_i, \tag{7}$$

where $(VEC)_i$ is the VEC for ith element and can be found at Ref. [66]. When VEC ≥ 8, FCC structure is more stable while VEC ≤ 6.87, BCC phases are more stable.

Therefore, multiple phase formation parameters can be calculated based on Eqs. (5-7) and the results are shown in Table 3. As can be seen, the FeCrNi alloy has a very high ΔS_{mix} (9.132 J·K⁻¹mol⁻¹), T_m (1906.6 K), and relatively small ΔH_{mix} (-4.3972 KJ·mol⁻¹), yielding the high value of Ω (3.9596). Accompanied with a low δ value (only 0.002), the result indicates the alloy can favorably form stable solid-solution phases. Additionally, the VEC of the alloy is calculated to be 7.97, which is very close to the theoretical criterion of forming a single FCC structure [66]. According to the neutron diffraction spectra (Fig. 3) and TEM results (Figs. 2 and 9), a single FCC solid solution phase was observed, in good agreement with the theoretical prediction.

Table 3 Multiple phase formation parameters, δ, ΔH_{mix}, ΔS_{mix}, and Ω of the FeCrNi alloy

Alloy	ΔS_{mix} [JK⁻¹mol⁻¹]	ΔH_{mix} [KJmol⁻¹]	T_m [K]	Ω	δ	VEC
FeCrNi	9.132	-4.3972	1906.6	3.9596	0.002	7.97

4.2 DFT results

According to the DFT results, up to the melting point, the free energy calculations considering magnetic corrections demonstrate that the FCC phase is stable at the equiatomic composition of FeCrNi alloy, which is in excellent agreement with the available experimental data. The atomistic configurations of medium-range and equiatomic FeCrNi alloys obtained from the present MC simulations of the $9 \times 9 \times 9$ FCC supercell for two temperatures: 300 and 2000 K are shown in Fig. 1a and 1b, respectively. At 2000 K, the configuration is more related to a disordered distribution of Fe, Cr, and Ni atoms over the simulation cell, whereas at 300 K, the configuration is more related to an ordering configuration. To understand this disorder-to-order transition, Fig. 10 shows the dependence of the first nearest-neighbor (1NN) SRO parameters of Fe-Cr, Fe-Ni, and C-Ni pairs as a function of temperature. At the high-temperature region, all the values of SRO trend to approach the zero values corresponding to random alloy configurations. For the

region of temperature lower than 1000 K, it is found that the SRO parameters for Fe-Cr and Fe-Ni are negative expressing the chemical interactions between these pairs in the ternary FeCrNi alloy. Between them, the SRO parameters for Fe-Cr pairs are more negative than those of Fe-Ni demonstrating a stronger chemical ordering between Fe and Cr. The SRO parameters between Cr and Ni are positive in this temperature range demonstrating that these two atoms did not like each other within the 1NN shell of the FCC lattice.

Fig. 1c and 1d show the $3 \times 3 \times 3$ supercell configurations used for DFT calculations of elastic constants in equiatomic FeCrNi alloys within the present work. They were generated by using combined first-principles CE Hamiltonian with exchange MC simulations at 300 and 2000 K. Space group symmetry of these configurations are found to be *P1* and *Pnnm*, respectively. The prediction of orthorhombic symmetry for the 300 K configuration demonstrates that the ordered structure obtained from the present theoretical study is strongly correlated with the SRO effects shown in Fig. 10 at low temperature for the medium-range FeCrNi alloy at equiatomic composition. It is worth noting that the point group symmetry of *Pnnm* crystal represents a subgroup of the tetragonal structure *P4/mmm* which has been previously predicted for intermetallic phase Fe_2CrNi from our DFT study in the FCC Fe-Cr-Ni system [35].

The elastic constants calculated by DFT for configurations generated by MC simulations at 300 and 2000 K MC are shown in Table 4. Note that for the high-temperature (2000 K) configurations with *P1* symmetry, the elastic constant values were computed by the new method outlined from Eqs. (3) and (4) where the 12 components from 21 independent elastic tensor components are negligible for the random alloy configuration. For the low-temperature configuration (300 K), DFT calculations provide 9 independent elastic constant values according to the orthorhombic group symmetry *Pnnm*. The optimized lattice constants from DFT calculations for the low-temperature configurations are a=3.5549Å, b=3.5486Å, and c=3.6264Å which are slightly different from the ones for a cubic cell. The corresponding values for high-temperature configurations are a=3.5385Å, b=3.5459Å, and c=3.5722Å. A larger lattice constant value at low temperature can be explained by magneto-volume effects due to high values of predicted magnetic moments in the ordered FeCrNi alloys. According to our DFT calculations, the average ferromagnetic moments of Fe and Ni sites are 2.1 and 0.16 μ_B, respectively, whereas an average anti-ferromagnetic moment of ±2.2 μ_B was found from Cr sites within the orthorhombic structure *Pnnm*. Note that the magnetic moment value predicted for the Fe site in the Fe_2CrNi structure is also found to be close to 2.1 μ_B [35]. For the high-temperature configuration, magnetic moments at different atomic sites are found to be randomly distributed and their average values are smaller than those predicted above for the ordered structure as expected. As it can be seen from Table 4, the DFT calculations were performed within different options, either with the lattice and ionic relaxations (denoted as "Relaxed") or without ionic relaxations (denoted as "Unrelaxed").

From the DFT results, it is found that elastic constants at high temperatures are smaller than the ones under low-temperature configurations, demonstrating the strong effect of disorder with respect to chemical ordering for the latter one. From Table 4, the predicted DFT elastic properties for the disordered configuration generated by MC simulations at 2000 K are in very good agreement with the experimental values measured in this work.

The elastic properties obtained by DFT are shown in Fig. 7i to 7l, which also closely resembles those measured experimentally. This strongly indicates that the prepared experimental FeCrNi alloy samples are more likely to be in a metastable state as a result of the fabrication (fast cooling after hot extrusion) without annealing treatment, which may prevent the formation of SROs and ordered intermetallic phase predicted by DFT calculations at a low-temperature regime [15,16]. This means that the SRO effects shown in Fig. 10 from our modeling work are absent in the present experimental alloys. The absence of the SRO effect is checked by the neutron diffraction results (Fig. 4) and it is found that no other diffuse superlattice peaks can be identified experimentally. Furthermore, this result is well supported by the APT analysis and the extensive HRTEM analysis (Fig. 2). SRO formation preferably occurred after long-time annealing at high temperatures. For example, in CrCoNi alloy, SROs were observed after annealing at 1000 °C for 120 h [16].

Table 4 Elastic constants and moduli predicted by DFT calculations and compared with experimental data. (More detailed comparison can be found in Table S2, the Supplementary Materials)

	FeCrNi	DFT 2000 K	DFT 2000 K	DFT 300 K	DFT 300 K	In situ Exp. 293 K	In situ Exp. 15 K
	Symmetry	$P1$	$P1$	$Pnnm$	$Pnnm$		
	K-points	$4 \times 4 \times 4$	$4 \times 4 \times 4$	$4 \times 4 \times 4$	$6 \times 6 \times 6$		
		Relaxed	Unrelaxed	Relaxed	Relaxed		
Elastic Constant [GPa]	C_{11}	210.79	222.45	239.41	237.44	225	220
	C_{12}	141.19	134.8	117.01	116.4	151	134
	C_{13}	136.06	142.6	136.48	137.24	-	-
	C_{22}	200.47	213.16	231.37	229.99	-	-
	C_{23}	127.42	132.09	109.34	108.92	-	-
	C_{33}	206.05	218.31	257.46	259.19	-	-
	C_{44}	123.42	125.36	163.14	163.46	123	127
	C_{55}	122.36	138.84	143.22	142.18	-	-
	C_{66}	122.19	131.67	141.19	140.99	-	-
	C' (average)	35.4	40.7	60.9	60.7	37.0	43.0
Young's Modulus [GPa]	E_{av}	180.83	199.81	248.02	247.12	187.95	201.8
Poisson's Ratio	P_{av}	0.3093	0.2962	0.2429	0.2433	0.3216	0.2932
Polycrystalline Moduli [GPa]	$B_{(VRH)}$	158.33	163.53	161.09	160.77	175.65	162.67
	$G_{(VRH)}$	74.57	82.45	103.62	103.27	76.17	82.35
	$E_{(VRH)}$	192.64	211.12	255.64	254.82	199.06	210.9

4.3 Yield strength modeling

For the FeNiCr MEA, the YS can be the accumulative result of several strength contributors including frictional stress (σ_{fr}), initial dislocation density (σ_{dis}), precipitate hardening (σ_{ppt}), grain boundary strengthening (σ_{gb}), and SRO strengthening (σ_{SRO}) [2]:

$$\sigma_{YS} = \sigma_{fr} + \sigma_{dis} + \sigma_{ppt} + \sigma_{gb} + \sigma_{SRO}. \tag{8}$$

First, the precipitation strengthening can be ignored in the present study. According to the neutron diffraction results shown in Fig. 4, during elastic deformation at both 293 and 15 K, the alloy keeps a single FCC phase, and no precipitates were detected except a small amount of Cr-rich phases at grain boundaries (Fig. 2c). The bright-field TEM images and corresponding SAED patterns (Fig. 2 and 9) did not reveal nano-precipitates. Next, we address the SRO hardening effects. On one hand, the HRTEM characterization in Fig. 2 indicated only a trace amount of SRO may be present. On the other hand, the strengthening effects of SRO can be very limited according to Ref. [67]. Therefore, the strengthening effects of trace SRO in the MEA can be neglected.

The strengthening contribution from forest dislocations can be evaluated by the classic Taylor hardening model [68]:

$$\sigma_{dis} = M\alpha Gb\sqrt{\rho}, \tag{9}$$

where M is the Taylor factor and equals 3.06 for an FCC polycrystalline matrix, α is a constant of 0.35 [69] related to the interaction strength between dislocations, G is the shear modulus, b is the Burger's vector, and ρ is the dislocation density. The neutron diffraction results indicate that the dislocation density of the virgin sample is around 6×10^{13} m^{-2} at both 293 and 15 K (Fig. 8b). According to Eq. (9), the strengthening effects from initial dislocations are ~164 MPa at 293 K and ~196 MPa at 15 K.

The strengthening effect of grain boundaries (σ_{gb}) can be calculated via the Hall-Petch equation. The grain boundary strengthening effect keeps a linear relationship with the inverse square root of average grain size [70]:

$$\sigma_{gb} = \sqrt{\frac{G(T)}{G(RT)}} K_{gb} d^{-1/2}, \tag{10}$$

where the Hall-Petch coefficient (K_{gb}) of 0.966 MPa·m$^{1/2}$ was used based on Ref. [6], $G(T)$ and $G(RT)$ are the shear modulus at a given temperature and room temperature, respectively. With the average grain size of ~23.4 µm, the grain boundaries contributed ~200 MPa (293 K) and ~218 MPa (15 K) to the yield stress.

Next, we address the lattice friction stress (σ_{fr}) of the alloy at the two temperatures. Note that the classical solid-solution strengthening mechanism is limited to the conventional ductile alloy systems where the dislocation movement can be inhibited by the strain field arising from the mismatch between discrete and solvent atoms [7]. The flexibility of dislocation lines enables them to bend to overcome the energy barriers and take on low-energy configurations. However, as the notion of "one principal element" was abandoned in MCAs, the constituent atoms with different sizes can be randomly distributed among the matrix, in which each elemental atom in the alloys can act as a solute. In this scenario, the traditional "solvent" lattice does not exist and the spacing distance between each energy barrier can be decreased significantly [4,18]. Thus, the traditional methods of depicting lattice friction stress and solution strengthening effects are no longer suitable for MCAs. According to Ref. [2], the MCAs can be treated as a stoichiometric compound with a fixed atomic ratio albeit disordered. Therefore, the traditional solid solution hardening

contribution can be included in the lattice friction effect, which can be more representative of the averaged lattice resistance provided by all types of constituent elements.

Recently, Varvenne et al. [18] proposed a general mechanistic solute strengthening theory (here named as the Varvenne-Luque-Curtin theory) for arbitrary MCAs, showing great success in predicting the YS of multiple HEAs and MEAs by correlating composition, temperature, and strain rate [19]. Different from traditional solute strengthening effects, the Varvenne-Luque-Curtin theory assumes the MCA is an effective-medium matrix having all the average properties of the alloy. Each substitutional element is treated as a solute embedded in the matrix and serves as local fluctuation. The strengthening effect then originates from the rising fluctuating interaction energies between dislocations and dense local fluctuations. To reduce the total potential energy, the dislocation adopts a wavy configuration and is locally pinned in a low-energy region. The representative wavy configuration of dislocations was observed in the slightly deformed samples at 15 K (as shown in Fig. S2, the Supplementary Materials), where the dislocation motion shows sluggish features, indicating high resistance originating from the pronounced lattice distortion in MCAs [16]. With the aid of stress-assisted thermal activation, the trapped dislocation can escape the adjacent energy well and reach the next low-energy region along the dislocation gliding plane. This theory calculated the zero-temperature flow stress (τ_{y0}) and fundamental zero-stress energy barrier (ΔE_b) at finite temperature (T) and finite strain-rate ($\dot{\varepsilon}$) [18]:

$$\tau_{y_0} = A_\tau \alpha_t^{-\frac{1}{3}} G \left(\frac{1+v}{1-v}\right)^{\frac{4}{3}} \left[\frac{\sum_n c_n \Delta V_n^2}{b^6}\right]^{\frac{2}{3}} \tag{11}$$

$$\Delta E_b = A_E \alpha_t^{\frac{1}{3}} G b^3 \left(\frac{1+v}{1-v}\right)^{\frac{2}{3}} \left[\frac{\sum_n c_n \Delta V_n^2}{b^6}\right]^{\frac{1}{3}}, \tag{12}$$

where $A_\tau = 0.04865[1 - \frac{(A-1)}{40}]$ and $A_E = 2.5785[1 - \frac{(A-1)}{80}]$ are two constants related to the core structure of FCC dislocations consisting of two separated partial dislocations accompanied with a correction for elastic anisotropy with the Zener anisotropy factor $A = \frac{2C_{44}}{(C_{11}-C_{12})}$. $\alpha_t = 0.125$ is a dimensionless line tension parameter for FCC alloys [19]. ΔV_n is the misfit volume of a type-n element at composition (c_n) in the alloy [4]:

$$\Delta V_n = \frac{\partial V_{alloy}}{\partial c_m} - \sum_m^N c_m \frac{\partial V_{alloy}}{\partial c_m}, \tag{13}$$

, where $V_{alloy} = V_{alloy}(c_1, c_2, \ldots, c_{N-1})$ is the atomic volume of the alloy and $\frac{\partial V_{alloy}}{\partial c_N} = 0$. The volume misfit can then be experimentally determined by measuring the lattice parameter evolution over a series of alloys [19]. It can also be computed precisely with the first-principles calculation, after replacing one type-n atom multiple times with a type-m atom at many different atomic environments [71]. In our case, we applied Vegard's law ($V_{alloy} = \sum_n c_n V_n$) to estimate the misfit volume [4,18]:

$$\Delta V_n = V_n - V_{alloy}, \tag{14}$$

18

where V_n is the apparent volume of the type-n element. Based on the experimental results on Ni, Ni-Cr, and Ni-Fe binary alloys from Ref. [18], the apparent atomic volumes of the three constituent elements Fe, Cr, and Ni were adapted to be 12.09, 12.27, and 10.94 Å^3, respectively.

At finite temperature T and finite strain-rate, Eq. (11) and (12) can be combined based on the standard thermal activation [72]:

$$\tau_y(T, \dot{\varepsilon}) = \tau_{y_0} exp\left(-\frac{1}{0.51}\frac{k_B T}{\Delta E_b(T)}ln\frac{\dot{\varepsilon}_0}{\dot{\varepsilon}}\right), \tag{15}$$

where the strain rate ($\dot{\varepsilon}$) of 8×10^{-5} s^{-1} was used in the present study, $\dot{\varepsilon}_0$ is a reference strain rate and a value of 10^4 s^{-1} was adapted according to Refs. [18,19], and k_B is the Boltzmann constant. Therefore, the uniaxial friction stress can then be calculated by multiplying the shear stress by the Taylor factor:

$$\sigma_{fr}(T, \dot{\varepsilon}) = M\tau_y(T, \dot{\varepsilon}). \tag{16}$$

Finally, with inputs obtained from the experiments (Tables 4 and 5), the lattice friction stress of the FeCrNi alloy was determined to be 316 and 629 MPa at 293 and 15 K, respectively.

According to Eq. (8), the YS of the alloy at 293 and 15 K can be estimated to be 680 and 1043 MPa, respectively. As compared in Table 5, the modeled strength shows acceptable agreement with the measured results at both temperatures. The calculation of strengthening contribution from lattice distortion based on the Varvenne-Luque-Curtin theory of random MCAs plays a critical role in understanding the strengthening mechanisms and can serve as a guideline in designing and optimizing new MCAs.

Table 5 The modeled and measured the strength of the alloy at different temperatures

	293 K	15 K
σ_{dis} [MPa]	164	196
σ_{gb} [MPa]	200	218
σ_{fr} [MPa]	316	629
Modeled σ_{YS} [MPa]	680	1043
Measured σ_{YS} [MPa]	651 ± 12	1092 ± 22

4.4 Plastic deformation

Generally, the large elongation of FCC alloys can be achieved via introducing extra strengthening mechanisms (such as TWIP and TRIP effects) [22]. The FeCrNi has high SFE and no TWIP or TRIP effects were observed when deformed. The high SFE of the FeCrNi MEA means that the activation of multiple strengthening mechanisms is impeded. Hence, the dislocation activity becomes the main strain contributor during the plastic deformation [11,22,59]. Even with the only dislocation strengthening for the FeCrNi, a notably good combination of strength and ductility was obtained. This result further augments recent research [73] showing that TWIP and TRIP are not necessarily required for extra-large ductility. The large ductility (48%) at 293 K might be attributed to divisive

slip systems activated and the high dislocation multiplication capacity of the alloy. According to the diffraction results (very low level of SFP, high SFE, and no twinning and phase transformation during deformation), together with the post-deformation TEM observations (Fig. 9), the dislocation motion and multiplication are the main strengthening resource and carrier of plasticity during plastic deformation.

Based on dislocation motions, the deformation procedure at 293 and 15 K was schematically compared in Fig. 11. At 15 K grain rotation from other orientations to (111)//LD developed much slower than that at 293 K (Fig. 8c and 8d). A similar phenomenon can also be observed in another MEA of CrCoNi during deforming at 15 K [56]. Grains orientated near (111)//LD were highly strained and dislocation entanglement forms more easily, leading to the deterioration of the ductility. Besides, the low temperature also impeded the dislocation motion, especially dislocation annihilation, contributing to the faster dislocation increment at 15 K (Fig. 8b) [22]. While at 293 K, the rapid growing texture endowed not-so-good-orientated grains with the ability to activate more slip systems thus providing extra strain carriers. This process can sustainably support dislocation multiplication, providing a stronger dislocation strengthening effect and improved ductility.

Based on the dislocation-dominated deformation mechanism, a constitutive model to depict the total flow stress (σ) of the alloy can be derived as follows:

$$\sigma = \sigma_{fr} + \sigma_{gb} + \sigma_{dis}. \tag{17}$$

The strengthening effect from dislocation can be determined by Eq. (9) and the dislocation density evolution (Fig. 8b). After yielding, the dislocation density increased almost linearly with the true stress at both temperatures. When deforming at 293 K to a true strain of 0.31, strengthening contribution from dislocations can reach 854 MPa. At 15 K, dislocations contributed 697 MPa at a true strain of 0.12. The accumulated strengthening contributions from different resources at 293 and 15 K according to Eq. (17) are compared with the measured flow stress at 293 and 15 K as shown in Fig. 12a and 12b, respectively. The model calculations agree very well with the experimental results.

5. Conclusions
In this study, we have investigated the deformation behaviors and strengthening mechanisms of an equiatomic ternary FeNiCr MEA at 293 K and 15 K. *In situ* neutron diffraction and theoretical simulations (DFT and dislocation slip system driven modeling) were synergistically employed to (i) map the microstructure evolution (e.g., lattice strain, SFP, and dislocation density); (ii) determine key mechanistic parameters (single crystal elastic constants and SFE) and (iii) confirm the strengthening mechanisms. The investigation leads to the following conclusions:

1. The equiatomic ternary FeNiCr alloy showed excellent strength-ductility balance at 293 K with YS of 651 ± 12 MPa, UTS of 1020 ± 3 MPa, and total elongation of $48 \pm 5\%$. At 15 K, ultrahigh YS of 1092 ± 22 MPa and UTS of 1451 ± 2 MPa were achieved, while the elongation decreased to $18 \pm 1\%$.

2. MC simulation predicts the formation of short-range ordering and Fe_2CrNi intermetallic. However, no short-range orderings were observed according to the neutron diffraction

spectra and APT. TEM analysis shows a very small amount of short-range ordering. This indicates that the alloy was at a metastable state and the SRO effect was almost absent possibly due to the sample fabrication technique used.

3. Single-crystal elastic constants and bulk elastic moduli were calculated from the neutron diffraction data, which agree well with the DFT simulation for the disordered configuration generated by MC simulations at 2000 K, but less well with the ordered configuration generated by MC at 300 K. This again suggests that the alloy produced was in a metastable configuration.

4. At both 293 and 15 K, the FeNiCr MEA showed high phase stability and maintained as an FCC solid solution during deformation. Meanwhile, it showed a very low level of stacking fault probability during deformation and had high SFE (63 ± 4 mJm^{-2} at 293 K and 47 ± 3 mJm^{-2} at 15 K), indicating its inability of producing massive stacking faults and introducing TWIP and TRIP effects. The *in situ* neutron diffraction data and TEM analysis confirmed that no TWIP or TRIP effects occurred when the alloy was deformed at both temperatures.

5. The high solute misfit volumes of the FeNiCr can effectively introduce severe lattice distortion, which substantially improves the yield strength, especially at extremely low-temperature conditions. Based on the Varenne-Luque-Curtin theory, the strengthening contribution from the lattice distortion was calculated. At 293 K, the friction stress, resulting from the lattice distortion, can contribute 316 MPa to the YS, while it increased significantly to 629 MPa at 15 K. Strengthening contributions from dislocation and grain boundaries were also calculated. And the sum of the three contributions agreed well with the measured yield strength at both temperatures.

6. During plastic deformation, dislocation motion and multiplication serve as the dominant deformation mechanism and the main strain carrier at 293 and 15 K. The as-fabricated samples had a low dislocation density of $\sim 6 \times 10^{13}$ m^{-2}. After yielding, dislocation density increased almost linearly with true stress.

CRediT authorship contribution statement
L. Tang: Data curation, Formal analysis, Visualization, Writing – original draft, Writing - Review & Editing. **F.Q. Jiang:** Investigation, Writing - Review & Editing. **J.S. Wróbel:** Software, Data curation, Writing - Review & Editing. **B. Liu:** Resources, Writing - Review & Editing. **S. Kabra:** Investigation, Writing – review & editing. **R.X. Duan:** Investigation, Writing – review & editing. **J.H. Luan:** Investigation, Writing – review & editing. **Z.B. Jiao:** Investigation, Writing – review & editing. **M.M. Attallah:** Supervision, Writing – review & editing. **D. Nguyen-Manh**: Software, Data curation, Writing – review & editing. **B. Cai:** Supervision, Conceptualization, Methodology, Formal analysis, Writing-Reviewing & Editing.

References

[1] J.W. Yeh, S.K. Chen, S.J. Lin, J.Y. Gan, T.S. Chin, T.T. Shun, C.H. Tsau, S.Y. Chang, Nanostructured high-entropy alloys with multiple principal elements: Novel alloy design concepts and outcomes, Adv. Eng. Mater. 6 (2004) 299–303. https://doi.org/10.1002/adem.200300567.

[2] Z. Wu, H. Bei, G.M. Pharr, E.P. George, Temperature dependence of the mechanical properties of equiatomic solid solution alloys with face-centered cubic crystal structures, Acta Mater. 81 (2014) 428–441. https://doi.org/10.1016/j.actamat.2014.08.026.

[3] B. Cai, B. Liu, S. Kabra, Y. Wang, K. Yan, P.D. Lee, Y. Liu, Deformation mechanisms of Mo alloyed FeCoCrNi high entropy alloy: In situ neutron diffraction, Acta Mater. 127 (2017) 471–480. https://doi.org/10.1016/j.actamat.2017.01.034.

[4] B. Yin, F. Maresca, W.A. Curtin, Vanadium is an optimal element for strengthening in both fcc and bcc high-entropy alloys, Acta Mater. 188 (2020) 486–491. https://doi.org/10.1016/j.actamat.2020.01.062.

[5] A.J. Zaddach, C. Niu, C.C. Koch, D.L. Irving, Mechanical properties and stacking fault energies of NiFeCrCoMn high-entropy alloy, Jom. 65 (2013) 1780–1789. https://doi.org/10.1007/s11837-013-0771-4.

[6] M. Schneider, G. Laplanche, Effects of temperature on mechanical properties and deformation mechanisms of the equiatomic CrFeNi medium-entropy alloy, Acta Mater. 204 (2020) 116470. https://doi.org/10.1016/j.actamat.2020.11.012.

[7] S.S. Sohn, A. Kwiatkowski da Silva, Y. Ikeda, F. Körmann, W. Lu, W.S. Choi, B. Gault, D. Ponge, J. Neugebauer, D. Raabe, Ultrastrong Medium-Entropy Single-Phase Alloys Designed via Severe Lattice Distortion, Adv. Mater. 31 (2019) 1–8. https://doi.org/10.1002/adma.201807142.

[8]   Z. Li, K.G. Pradeep, Y. Deng, D. Raabe, C.C. Tasan, Metastable high-entropy dual-phase alloys overcome the strength-ductility trade-off, Nature. 534 (2016) 227–230. https://doi.org/10.1038/nature17981.

[9]   B. Gludovatz, A. Hohenwarter, D. Catoor, E.H. Chang, E.P. George, R.O. Ritchie, A fracture-resistant high-entropy alloy for cryogenic applications, Science (80-.). 345 (2014) 1153–1159. https://doi.org/10.1126/science.1254581.

[10]   B. Gludovatz, A. Hohenwarter, K.V.S.S. Thurston, H. Bei, Z. Wu, E.P. George, R.O. Ritchie, Exceptional damage-tolerance of a medium-entropy alloy CrCoNi at cryogenic temperatures, Nat. Commun. 7 (2016) 10602. https://doi.org/10.1038/ncomms10602.

[11]   L. Tang, K. Yan, B. Cai, Y. Wang, B. Liu, S. Kabra, M.M. Attallah, Y. Liu, Deformation mechanisms of FeCoCrNiMo0.2 high entropy alloy at 77 and 15 K, Scr. Mater. 178 (2020) 166–170. https://doi.org/10.1016/j.scriptamat.2019.11.026.

[12]   M. Naeem, H. He, F. Zhang, H. Huang, S. Harjo, T. Kawasaki, B. Wang, S. Lan, Z. Wu, F. Wang, Y. Wu, Z. Lu, Z. Zhang, C.T. Liu, X.L. Wang, Cooperative deformation in high-entropy alloys at ultralow temperatures, Sci. Adv. 6 (2020). https://doi.org/10.1126/sciadv.aax4002.

[13]   Y. Wang, B. Liu, K. Yan, M. Wang, S. Kabra, Y.L. Chiu, D. Dye, P.D. Lee, Y. Liu, B. Cai, Probing deformation mechanisms of a FeCoCrNi high-entropy alloy at 293 and 77 K using in situ neutron diffraction, Acta Mater. 154 (2018) 79–89. https://doi.org/10.1016/j.actamat.2018.05.013.

[14]   J. Ding, Q. Yu, M. Asta, R.O. Ritchie, Tunable stacking fault energies by tailoring local chemical order in CrCoNi medium-entropy alloys, Proc. Natl. Acad. Sci. U. S. A. 115 (2018) 8919–8924. https://doi.org/10.1073/pnas.1808660115.

[15]   X. Chen, Q. Wang, Z. Cheng, M. Zhu, H. Zhou, P. Jiang, L. Zhou, Q. Xue, F. Yuan, J. Zhu, X. Wu, E. Ma, Direct observation of chemical short-range order in a medium-entropy alloy, Nature. 592 (2021) 712–716. https://doi.org/10.1038/s41586-021-03428-z.

[16]   R. Zhang, S. Zhao, J. Ding, Y. Chong, T. Jia, C. Ophus, M. Asta, R.O. Ritchie, A.M. Minor, Short-range order and its impact on the CrCoNi medium-entropy alloy, Nature. 581 (2020) 283–287. https://doi.org/10.1038/s41586-020-2275-z.

[17]   Z. Wu, Y. Gao, H. Bei, Thermal activation mechanisms and Labusch-type strengthening analysis for a family of high-entropy and equiatomic solid-solution alloys, Acta Mater. 120 (2016) 108–119. https://doi.org/10.1016/j.actamat.2016.08.047.

[18]   C. Varvenne, A. Luque, W.A. Curtin, Theory of strengthening in fcc high entropy alloys, Acta Mater. 118 (2016) 164–176. https://doi.org/10.1016/j.actamat.2016.07.040.

[19]   B. Yin, S. Yoshida, N. Tsuji, W.A. Curtin, Yield strength and misfit volumes of NiCoCr and implications for short-range-order, Nat. Commun. 11 (2020) 2507.

https://doi.org/10.1038/s41467-020-16083-1.

[20] A. Fu, B. Liu, W. Lu, B. Liu, J. Li, Q. Fang, Z. Li, Y. Liu, A novel supersaturated medium entropy alloy with superior tensile properties and corrosion resistance, Scr. Mater. 186 (2020) 381–386. https://doi.org/10.1016/j.scriptamat.2020.05.023.

[21] G. Bonny, D. Terentyev, R.C. Pasianot, S. Poncé, A. Bakaev, Interatomic potential to study plasticity in stainless steels: The FeNiCr model alloy, Model. Simul. Mater. Sci. Eng. 19 (2011). https://doi.org/10.1088/0965-0393/19/8/085008.

[22] L. Tang, L. Wang, M. Wang, H. Liu, S. Kabra, Y. Chiu, B. Cai, Synergistic deformation pathways in a TWIP steel at cryogenic temperatures: In situ neutron diffraction, Acta Mater. 200 (2020) 943–958. https://doi.org/10.1016/j.actamat.2020.09.075.

[23] G. Kresse, J. Furthmüller, Efficient iterative schemes for ab initio total-energy calculations using a plane-wave basis set, Phys. Rev. B. 54 (1996) 11169–11186. https://doi.org/10.1103/PhysRevB.54.11169.

[24] G. Kresse, J. Furthmüller, Efficiency of ab-initio total energy calculations for metals and semiconductors using a plane-wave basis set, Comput. Mater. Sci. 6 (1996) 15–50. https://doi.org/10.1016/0927-0256(96)00008-0.

[25] J.P. Perdew, K. Burke, M. Ernzerhof, Generalized gradient approximation made simple, Phys. Rev. Lett. 77 (1996) 3865–3868. https://doi.org/10.1103/PhysRevLett.77.3865.

[26] H.J. Monkhorst, J.D. Pack, Special points for Brillouin-zone integrations, Phys. Rev. B. 13 (1976) 5188–5192. https://doi.org/10.1103/PhysRevB.13.5188.

[27] D. Nguyen-Manh, D.G. Pettifor, G. Shao, A.P. Miodownik, A. Pasturel, Metastability of the ω-phase in transition-metal aluminides: First-principles structural predictions, Philos. Mag. A Phys. Condens. Matter, Struct. Defects Mech. Prop. 74 (1996) 1385–1397. https://doi.org/10.1080/01418619608240730.

[28] D. Nguyen-Manh, D.G. Pettifor, Electronic structure, phase stability and elastic moduli of AB transition metal aluminides, Intermetallics. 7 (1999) 1095–1106. https://doi.org/10.1016/S0966-9795(99)00040-0.

[29] D. Nguyen-Manh, D.G. Pettifor, D. Kim, M.H. Loretto, Origin of O-phase and pseudo-twinning in Ti-Al-Nb alloys: a first-principles study, Gamma Titan. Alum. Kim, Y.-W., Dimiduk, DM, Loretto, MH, Eds. (1999) 175–182.

[30] D. Nguyen-Manh, V. Vitek, A.P. Horsfield, Environmental dependence of bonding: A challenge for modelling of intermetallics and fusion materials, Prog. Mater. Sci. 52 (2007) 255–298. https://doi.org/10.1016/j.pmatsci.2006.10.010.

[31] M. Muzyk, D. Nguyen-Manh, K.J. Kurzydłowski, N.L. Baluc, S.L. Dudarev, Phase stability, point defects, and elastic properties of W-V and W-Ta alloys, Phys. Rev. B - Condens. Matter Mater. Phys. 84 (2011) 104115. https://doi.org/10.1103/PhysRevB.84.104115.

[32] J. Wróbel, L.G. Hector, W. Wolf, S.L. Shang, Z.K. Liu, K.J. Kurzydłowski, Thermodynamic and mechanical properties of lanthanum-magnesium phases from density functional theory, J. Alloys Compd. 512 (2012) 296–310. https://doi.org/10.1016/j.jallcom.2011.09.085.

[33] L. Vitos, P.A. Korzhavyi, B. Johansson, Elastic Property Maps of Austenitic Stainless Steels, Phys. Rev. Lett. 88 (2002) 4. https://doi.org/10.1103/PhysRevLett.88.155501.

[34] N. Al-Zoubi, Elastic parameters of paramagnetic fe–20cr–20ni-based alloys: A first-principles study, Metals (Basel). 9 (2019) 792. https://doi.org/10.3390/met9070792.

[35] J.S. Wróbel, D. Nguyen-Manh, M.Y. Lavrentiev, M. Muzyk, S.L. Dudarev, Phase stability of ternary fcc and bcc Fe-Cr-Ni alloys, Phys. Rev. B - Condens. Matter Mater. Phys. 91 (2015) 024108. https://doi.org/10.1103/PhysRevB.91.024108.

[36] J.M. Cowley, An Approximate Theory of Order in Alloys, Phys. Rev. 77 (1950) 669–675. https://doi.org/10.1103/PhysRev.77.669.

[37] B.E. Warren, X-ray Diffraction, Courier Corporation, 1990.

[38] A. Fernández-Caballero, J.S. Wróbel, P.M. Mummery, D. Nguyen-Manh, Short-Range Order in High Entropy Alloys: Theoretical Formulation and Application to Mo-Nb-Ta-V-W System, J. Phase Equilibria Diffus. 38 (2017) 391–403. https://doi.org/10.1007/s11669-017-0582-3.

[39] A. Fernández-Caballero, M. Fedorov, J. Wróbel, P. Mummery, D. Nguyen-Manh, Configurational Entropy in Multicomponent Alloys: Matrix Formulation from Ab Initio Based Hamiltonian and Application to the FCC Cr-Fe-Mn-Ni System, Entropy. 21 (2019) 68. https://doi.org/10.3390/e21010068.

[40] M. Fedorov, J.S. Wróbel, A. Fernández-Caballero, K.J. Kurzydłowski, D. Nguyen-Manh, Phase stability and magnetic properties in fcc Fe-Cr-Mn-Ni alloys from first-principles modeling, Phys. Rev. B. 101 (2020) 174416. https://doi.org/10.1103/PhysRevB.101.174416.

[41] D. Sobieraj, J.S. Wróbel, T. Rygier, K.J. Kurzydłowski, O. El Atwani, A. Devaraj, E. Martinez Saez, D. Nguyen-Manh, Chemical short-range order in derivative Cr-Ta-Ti-V-W high entropy alloys from the first-principles thermodynamic study, Phys. Chem. Chem. Phys. 22 (2020) 23929–23951. https://doi.org/10.1039/d0cp03764h.

[42] M. Łopuszyński, J.A. Majewski, Ab initio calculations of third-order elastic constants and related properties for selected semiconductors, Phys. Rev. B - Condens. Matter Mater. Phys. 76 (2007) 045202. https://doi.org/10.1103/PhysRevB.76.045202.

[43] D. Holec, M. Friák, J. Neugebauer, P.H. Mayrhofer, Trends in the elastic response of binary early transition metal nitrides, Phys. Rev. B. 85 (2012) 64101. https://doi.org/10.1103/PhysRevB.85.064101.

[44] M.A. Caro, S. Schulz, E.P. O'Reilly, Comparison of stress and total energy methods for calculation of elastic properties of semiconductors, J. Phys. Condens. Matter. 25

(2013) 025803. https://doi.org/10.1088/0953-8984/25/2/025803.

[45] J.S. Wróbel, M.R. Zemła, D. Nguyen-Manh, P. Olsson, L. Messina, C. Domain, T. Wejrzanowski, S.L. Dudarev, Elastic dipole tensors and relaxation volumes of point defects in concentrated random magnetic Fe-Cr alloys, Comput. Mater. Sci. 194 (2021) 110435. https://doi.org/https://doi.org/10.1016/j.commatsci.2021.110435.

[46] R. Hill, The elastic behaviour of a crystalline aggregate, Proc. Phys. Soc. Sect. A. 65 (1952) 349–354. https://doi.org/10.1088/0370-1298/65/5/307.

[47] M.J. Hÿtch, E. Snoeck, R. Kilaas, Quantitative measurement of displacement and strain fields from HREM micrographs, Ultramicroscopy. 74 (1998) 131–146. https://doi.org/10.1016/S0304-3991(98)00035-7.

[48] J.Y. He, W.H. Liu, H. Wang, Y. Wu, X.J. Liu, T.G. Nieh, Z.P. Lu, Effects of Al addition on structural evolution and tensile properties of the FeCoNiCrMn high-entropy alloy system, Acta Mater. 62 (2014) 105–113. https://doi.org/10.1016/j.actamat.2013.09.037.

[49] J. Liu, Y. Jin, X. Fang, C. Chen, Q. Feng, X. Liu, Y. Chen, T. Suo, F. Zhao, T. Huang, H. Wang, X. Wang, Y. Fang, Y. Wei, L. Meng, J. Lu, W. Yang, Dislocation Strengthening without Ductility Trade-off in Metastable Austenitic Steels, Sci. Rep. 6 (2016) 1–9. https://doi.org/10.1038/srep35345.

[50] Z. Li, C.C. Tasan, K.G. Pradeep, D. Raabe, A TRIP-assisted dual-phase high-entropy alloy: Grain size and phase fraction effects on deformation behavior, Acta Mater. 131 (2017) 323–335. https://doi.org/10.1016/j.actamat.2017.03.069.

[51] H. Huang, Y. Wu, J. He, H. Wang, X. Liu, K. An, W. Wu, Z. Lu, Phase-Transformation Ductilization of Brittle High-Entropy Alloys via Metastability Engineering, Adv. Mater. 29 (2017) 1–7. https://doi.org/10.1002/adma.201701678.

[52] L. Lilensten, J.P. Couzinié, J. Bourgon, L. Perrière, G. Dirras, F. Prima, I. Guillot, Design and tensile properties of a bcc Ti-rich high-entropy alloy with transformation-induced plasticity, Mater. Res. Lett. 5 (2017) 110–116. https://doi.org/10.1080/21663831.2016.1221861.

[53] O.N. Senkov, S.L. Semiatin, Microstructure and properties of a refractory high-entropy alloy after cold working, J. Alloys Compd. 649 (2015) 1110–1123. https://doi.org/10.1016/j.jallcom.2015.07.209.

[54] G. Dirras, L. Lilensten, P. Djemia, M. Laurent-Brocq, D. Tingaud, J.P. Couzinié, L. Perrière, T. Chauveau, I. Guillot, Elastic and plastic properties of as-cast equimolar TiHfZrTaNb high-entropy alloy, Mater. Sci. Eng. A. 654 (2016) 30–38. https://doi.org/10.1016/j.msea.2015.12.017.

[55] S. Sheikh, S. Shafeie, Q. Hu, J. Ahlström, C. Persson, J. Veselý, J. Zýka, U. Klement, S. Guo, Alloy design for intrinsically ductile refractory high-entropy alloys, J. Appl. Phys. 120 (2016). https://doi.org/10.1063/1.4966659.

[56] H. He, M. Naeem, F. Zhang, Y. Zhao, S. Harjo, T. Kawasaki, B. Wang, X. Wu, S. Lan, Z. Wu, W. Yin, Y. Wu, Z. Lu, J.J. Kai, C.T. Liu, X.L. Wang, Stacking Fault

Driven Phase Transformation in CrCoNi Medium Entropy Alloy, Nano Lett. 21 (2021) 1419–1426. https://doi.org/10.1021/acs.nanolett.0c04244.

[57] J. Sas, K.P. Weiss, A. Jung, The Mechanical and material properties of 316LN austenitic stainless steel for the fusion application in cryogenic temperatures, IOP Conf. Ser. Mater. Sci. Eng. 102 (2015). https://doi.org/10.1088/1757-899X/102/1/012003.

[58] C. Lee, G. Kim, Y. Chou, B.L. Musicó, M.C. Gao, K. An, G. Song, Y.C. Chou, V. Keppens, W. Chen, P.K. Liaw, Temperature dependence of elastic and plastic deformation behavior of a refractory high-entropy alloy, Sci. Adv. 6 (2020) eaaz4748. https://doi.org/10.1126/sciadv.aaz4748.

[59] S. Curtze, V.-T.T. Kuokkala, Dependence of tensile deformation behavior of TWIP steels on stacking fault energy, temperature and strain rate, Acta Mater. 58 (2010) 5129–5141. https://doi.org/10.1016/j.actamat.2010.05.049.

[60] L. Vitos, J.O. Nilsson, B. Johansson, Alloying effects on the stacking fault energy in austenitic stainless steels from first-principles theory, Acta Mater. 54 (2006) 3821–3826. https://doi.org/10.1016/j.actamat.2006.04.013.

[61] C.B. Carter, S.M. Holmes, The stacking-fault energy of nickel, Philos. Mag. A J. Theor. Exp. Appl. Phys. 35 (1977) 1161–1172. https://doi.org/10.1080/14786437708232942.

[62] T. Ungár, S. Ott, P.G. Sanders, A. Borbély, J.R. Weertman, Dislocations, grain size and planar faults in nanostructured copper determined by high resolution X-ray diffraction and a new procedure of peak profile analysis, Acta Mater. 46 (1998) 3693–3699. https://doi.org/10.1016/S1359-6454(98)00001-9.

[63] W.F. Hosford, Mechanical Behavior of Materials, Cambridge University Press, Cambridge, 2005. https://doi.org/DOI: 10.1017/CBO9780511810930.

[64] X. Yang, Y. Zhang, Prediction of high-entropy stabilized solid-solution in multi-component alloys, Mater. Chem. Phys. 132 (2012) 233–238. https://doi.org/10.1016/j.matchemphys.2011.11.021.

[65] M. Zhang, L.G. Hector, Y. Guo, M. Liu, L. Qi, First-principles search for alloying elements that increase corrosion resistance of Mg with second-phase particles of transition metal impurities, Comput. Mater. Sci. 165 (2019) 154–166. https://doi.org/10.1016/j.commatsci.2019.04.018.

[66] S. Guo, C.T. Liu, Phase stability in high entropy alloys: Formation of solid-solution phase or amorphous phase, Prog. Nat. Sci. Mater. Int. 21 (2011) 433–446. https://doi.org/10.1016/S1002-0071(12)60080-X.

[67] R. Zhang, S. Zhao, C. Ophus, Y. Deng, S.J. Vachhani, B. Ozdol, R. Traylor, K.C. Bustillo, J.W. Morris, D.C. Chrzan, Direct imaging of short-range order and its impact on deformation in Ti-6Al, Sci. Adv. 5 (2019) eaax2799.

[68] O. Bouaziz, S. Allain, C. Scott, Effect of grain and twin boundaries on the hardening mechanisms of twinning-induced plasticity steels, Scr. Mater. 58 (2008) 484–487.

https://doi.org/10.1016/j.scriptamat.2007.10.050.

[69] R. Madec, B. Devincre, L.P. Kubin, From Dislocation Junctions to Forest Hardening, Phys. Rev. Lett. 89 (2002) 1–4. https://doi.org/10.1103/PhysRevLett.89.255508.

[70] J.P. Hirth, J. Lothe Theory of dislocations, 1982.

[71] B. Yin, W.A. Curtin, First-principles-based prediction of yield strength in the RhIrPdPtNiCu high-entropy alloy, Npj Comput. Mater. 5 (2019) 1–7. https://doi.org/10.1038/s41524-019-0151-x.

[72] G.P.M. Leyson, L.G. Hector, W.A. Curtin, Solute strengthening from first principles and application to aluminum alloys, Acta Mater. 60 (2012) 3873–3884. https://doi.org/10.1016/j.actamat.2012.03.037.

[73] Z.C. Luo, M.X. Huang, Revisit the role of deformation twins on the work-hardening behaviour of twinning-induced plasticity steels, Scr. Mater. 142 (2018) 28–31. https://doi.org/10.1016/j.scriptamat.2017.08.017.

List of Tables

Table 1 Uniaxial tensile properties of the FeCrNi alloy deformed at 293 K and 15 K

Table 2 Experimentally measured elastic properties of the FeCrNi alloy at different temperatures

Table 3 Multiple phase formation parameters, δ, ΔH_{mix}, ΔS_{mix}, and Ω of the FeCrNi alloy

Table 4 Elastic constants and moduli predicted by DFT calculations and compared with experimental data.

Table 5 The modeled and measured the strength of the alloy at different temperatures

List of Figures

Fig. 1 Monte-Carlo simulations of FCC supercell configurations for equiatomic FeCrNi alloys with different sizes and temperatures using DFT based CE Hamiltonian: (a) 9 × 9 × 9, 300 K; (b) 9 × 9 × 9, 2000 K; (c) 3 × 3 × 3, 300 K; (d) 3 × 3 × 3, 2000 K. The color code for Fe atoms is orange, Cr: blue and Ni: grey

Fig. 2 Microstructure characterization of the virgin FeCrNi sample: (a) EBSD map (inverse pole figure) perpendicular to extrusion direction (ED); (b) Band contrast map overlapped with boundaries map of (a), the red, black, and green lines in the boundary map represents the low-angle grain boundaries (LAGBs), high-angle grain boundaries (HAGBs), and annealing twin boundaries (TBs, Σ3 {111}); (c) SEM-BSE images and

corresponding elemental mapping of Fe, Cr, and Ni obtained from EDX analysis; (d) typical bright TEM image and SAED pattern taken along [110] zone axes; (e) Three-dimension APT tip reconstructions of Fe, Cr, and Ni atoms; (f) Frequency distribution analysis of the three constituent elements and corresponding parameters used for qualifying the fit; (g) and (h) HRSTEM images and the corresponding FFT images of the alloy taken from [110] and [112] zone axis, respectively.

Fig. 3 (a) Engineering and true stress-strain curves of the alloy deformed at 293 and 15 K; (b) Yield strength-uniform elongation comparison among current FeCrNi MEA, several high-strength steels, and single or multi-phase MEAs/HEAs[2,3,8,10,48-55].

Fig. 4 *In situ* neutron diffraction spectra collected during deforming at (a) 293 K and (b) 15 K.

Fig. 5 Lattice strain evolution of crystallographic planes of {111}, {200}, {220}, {311}, and {222} from axial and radial directions during deforming at (a) 293 K and (b) 15 K.

Fig. 6 The reciprocal diffraction elastic moduli ($1/E_{hkl}$ and v_{hkl}/E_{hkl}) plotted as a function of the elastic anisotropy factor, A_{hkl}, which were obtained from the experimental measured (Mea.) elastic lattice strain and fitted by Kroner, Voigt, and Reuss models at (a) 293 K and (b) 15 K, respectively.

Fig. 7 Elastic properties of the FeNiCr alloy at 293 K determined via *in situ* neutron diffraction measurements (a-h) and DFT calculations (i-l). The magnitude with respect to the directions in three dimensions for: (a)(i) Young's modulus, (b)(j) shear modulus, (c)(k) Poisson's ratio, and (d)(l) linear compressibility, respectively. The maximum and minimum values of shear modulus and Poisson's ratio are represented by two surfaces. The magnitude with respect to directions of XY, XZ, and YZ plane for (e) Young's modulus, (f) shear modulus, (g) linear compressibility, and (h) Poisson's ratio, respectively. The maximum and minimum values of shear modulus and Poisson's ratio are represented by dashed and solid lines, respectively.

Fig. 8 Microstructure evolution during straining at 293 K and 15 K: (a) comparison of stacking fault probability (SFP) evolution between the FeNiCr alloy and FeCoCrNiMo$_{0.2}$ alloy at different temperatures; (b) dislocation density evolution of the FeNiCr alloy during deformation; The normalized peak intensity evolution of {111}, {200}, {220}, {311}, and {222} of the FeNiCr alloy during deforming at (c) 293 K and (d) 15 K.

Fig. 9 Deformed microstructure of the alloy at different strain levels and different temperatures, 293 K and 15 K: (a) typical bright-field TEM image (at the strain of ~0.1, 293 K) and corresponding SAED pattern of the area marked by the yellow dashed circle; (b)(c) bright-field TEM images and corresponding SAED patterns at the strain of ~0.1 and near the fracture surface at 293 K, respectively; (d) bright-field TEM image and corresponding SAED pattern at the strain of ~0.1, 15 K; (e)(f) HAADF-STEM images of the deformed structure at the strain of ~0.1 and near the fracture surface at 15 K, respectively; (g) HRTEM image of the dislocation tangling zone in (e); (h) The geometric phase analysis (GPA) conducted on (g).

Fig. 10 Dependence of SRO parameters as a function of temperature between the three different pairs in equiatomic FeCrNi alloys.

Fig. 11 Schematic illustration of the deformation procedure at 293 and 15 K.

Fig. 12 The comparison between the calculated strength originating from different strengthening resources and the measured total flow stress at (a) 293 K and (b) 15 K.
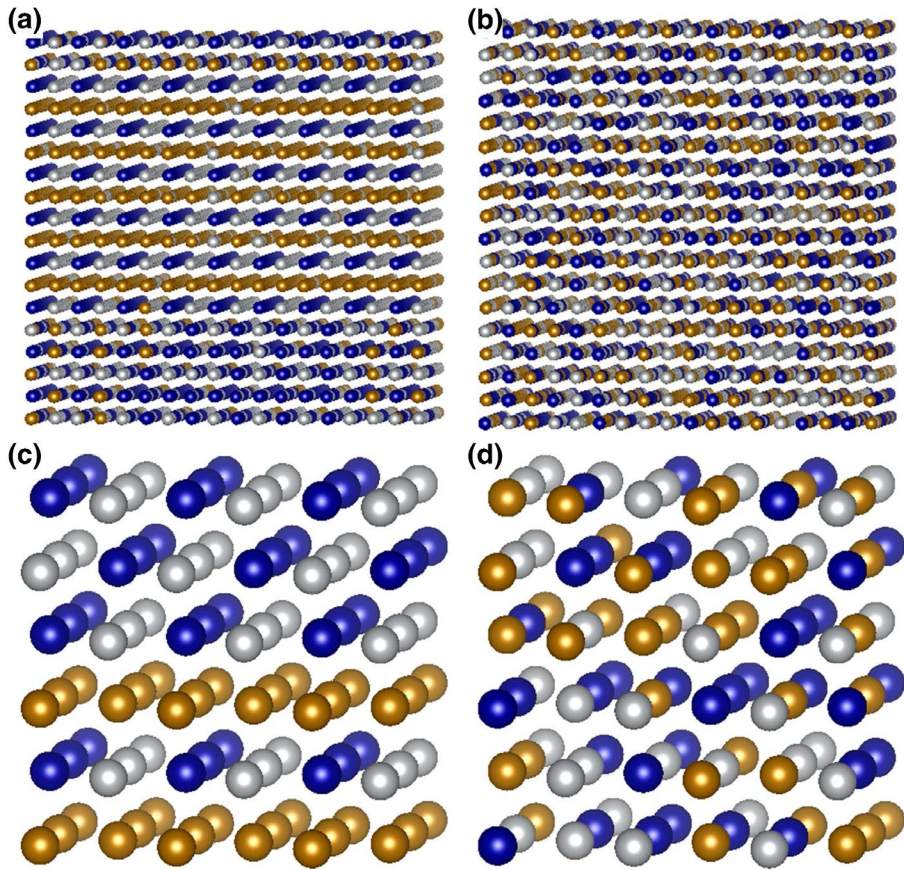
Fig. 1 Monte-Carlo simulations of FCC supercell configurations for equiatomic FeCrNi alloys with different sizes and temperatures using DFT based CE Hamiltonian: (a) 9 × 9 × 9, 300 K; (b) 9 × 9 × 9, 2000 K; (c) 3 × 3 × 3, 300 K; (d) 3 × 3 × 3, 2000 K. The color code for Fe atoms is orange, Cr: blue and Ni: grey
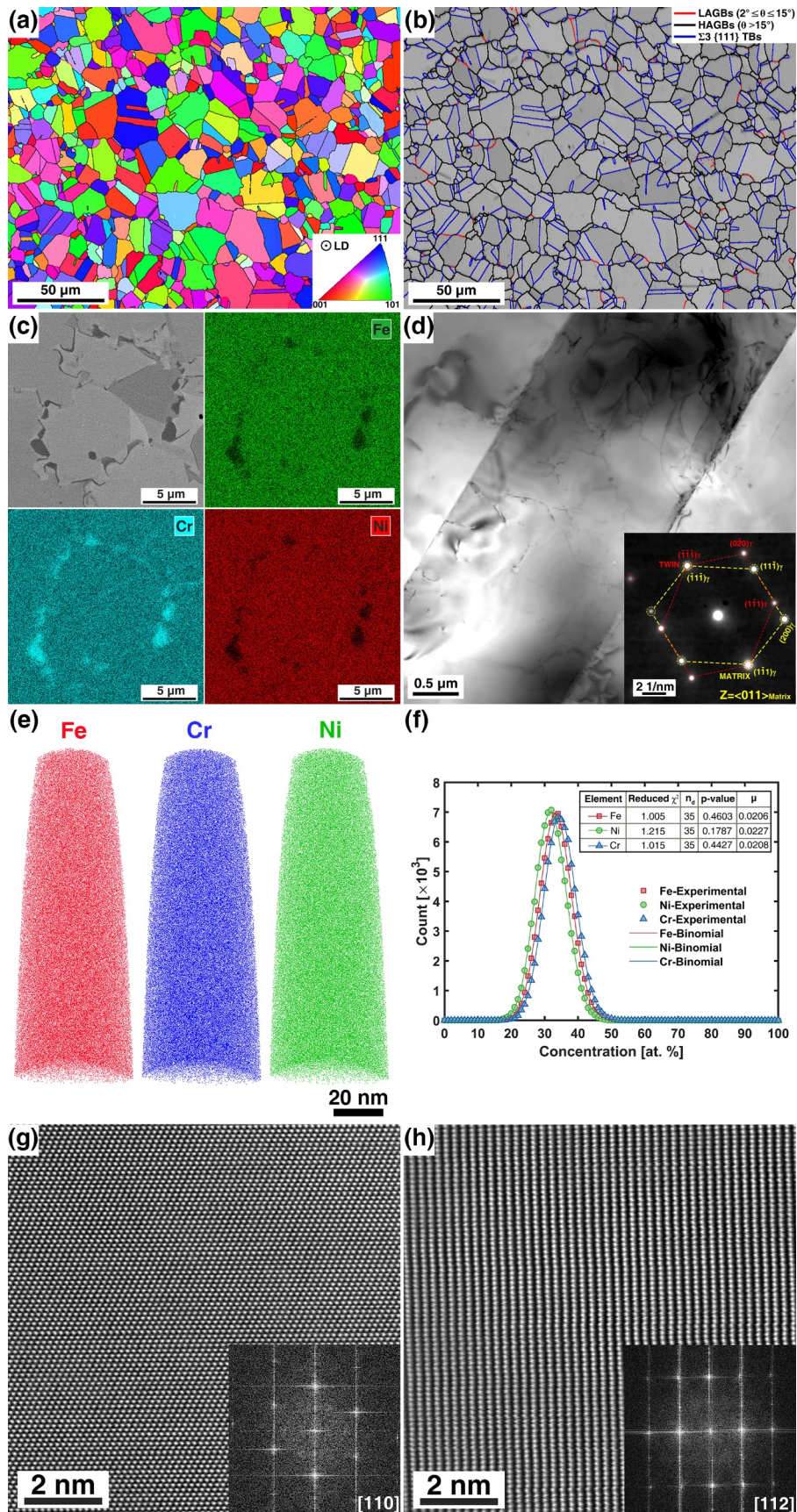
Fig. 2 Microstructure characterization of the virgin FeCrNi sample: (a) EBSD map (inverse pole figure) perpendicular to loading direction (LD); (b) Band contrast map overlapped with boundaries map of (a), the red, black, and green lines in the boundary map represents the low-angle grain boundaries (LAGBs), high-angle grain boundaries (HAGBs), and annealing twin boundaries (TBs, Σ3 {111}); (c) SEM-BSE images and corresponding elemental mapping of Fe, Cr, and Ni obtained from EDX analysis; (d) typical bright TEM image and SAED pattern taken along [110] zone axes; (e) Three-dimension APT tip reconstructions of Fe, Cr, and Ni atoms; (f) Frequency distribution analysis of the three constituent elements and corresponding parameters used for qualifying the fit; (g) and (h) HRSTEM images and the corresponding FFT images of the alloy taken from [110] and [112] zone axis, respectively.
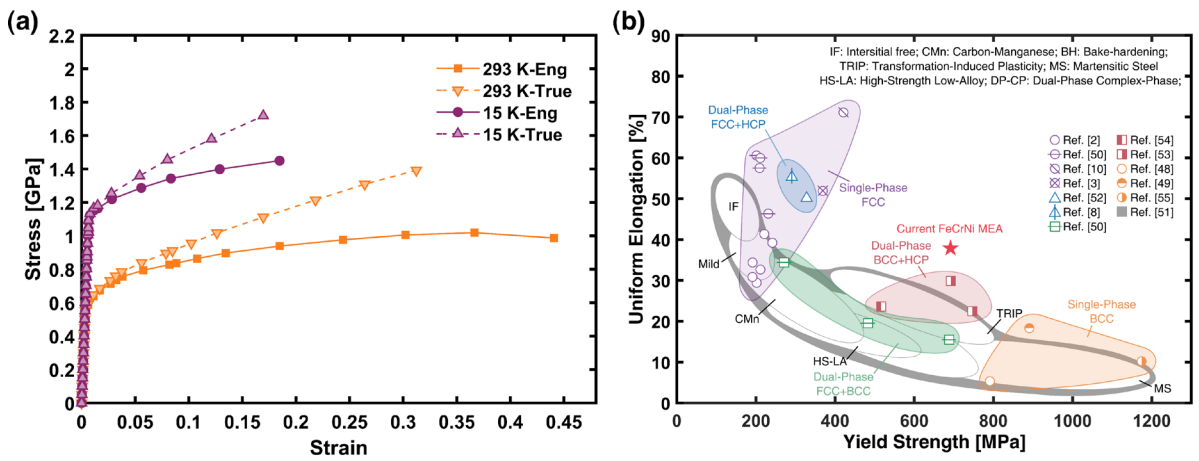
Fig. 3 (a) Engineering and true stress-strain curves of the alloy deformed at 293 and 15 K; (b) Yield strength-uniform elongation comparison among current FeCrNi MEA, several high-strength steels and single or multi-phase MEAs/HEAs[2,3,8,10,48-55].
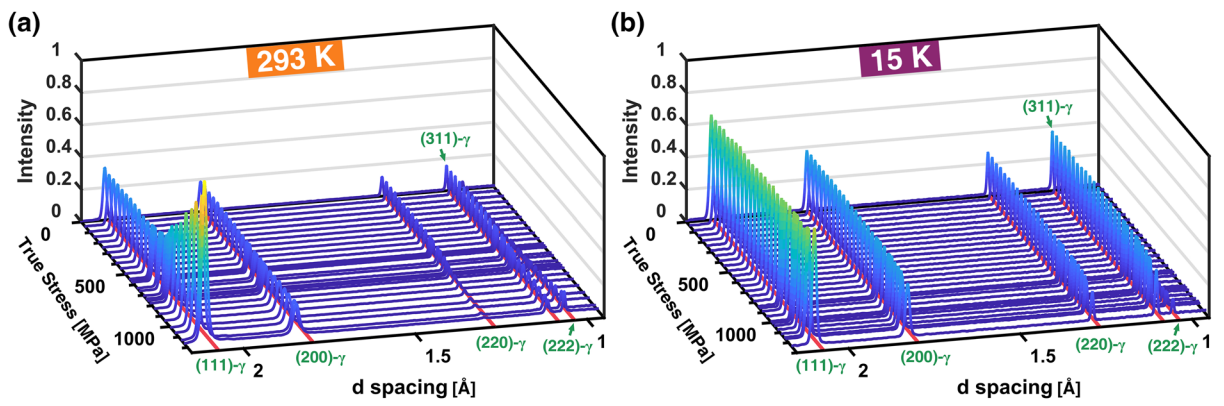
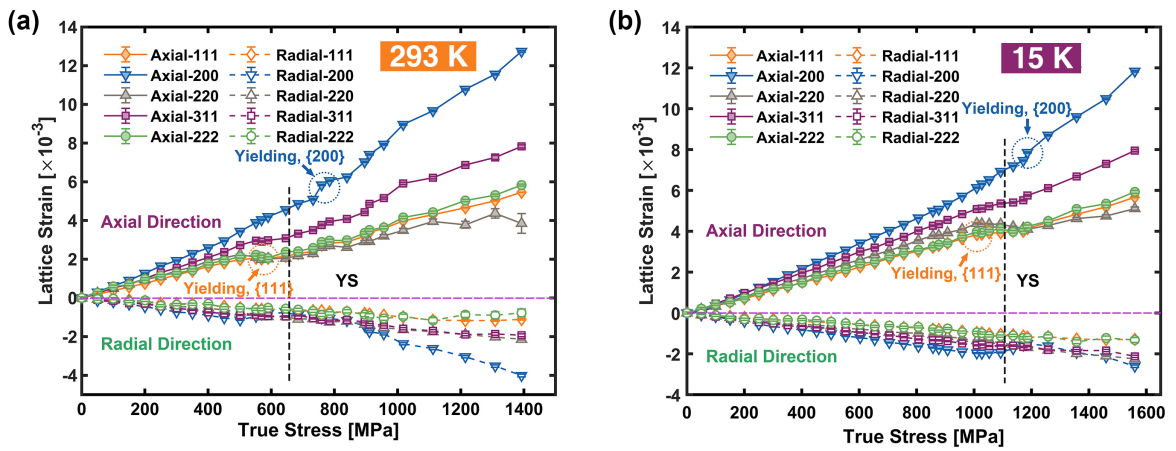**Fig. 4** *In situ* neutron diffraction spectra collected during deforming at (a) 293 K and (b) 15 K.

Fig. 5 Lattice strain evolution of crystallographic planes of {111}, {200}, {220}, {311}, and {222} from axial and radial directions during deforming at (a) 293 K and (b) 15 K.
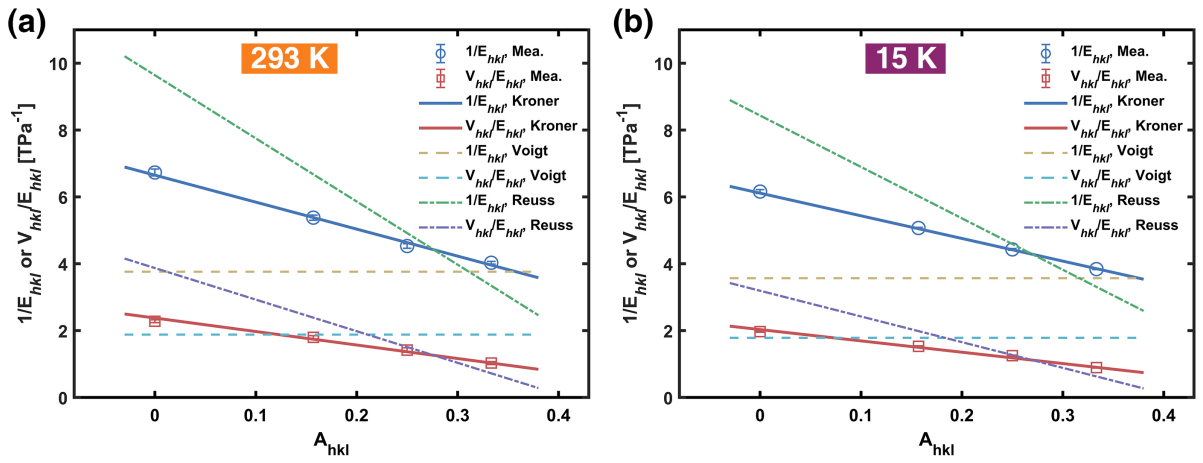
Fig. 6 The reciprocal diffraction elastic moduli ($1/\mathrm{E}_{hkl}$ and v_{hkl}/E_{hkl}) plotted as a function of the elastic anisotropy factor, A_{hkl}, which were obtained from the experimental measured (Mea.) elastic lattice strain and fitted by Kroner, Voigt, and Reuss models at (a) 293 K and (b) 15 K, respectively.
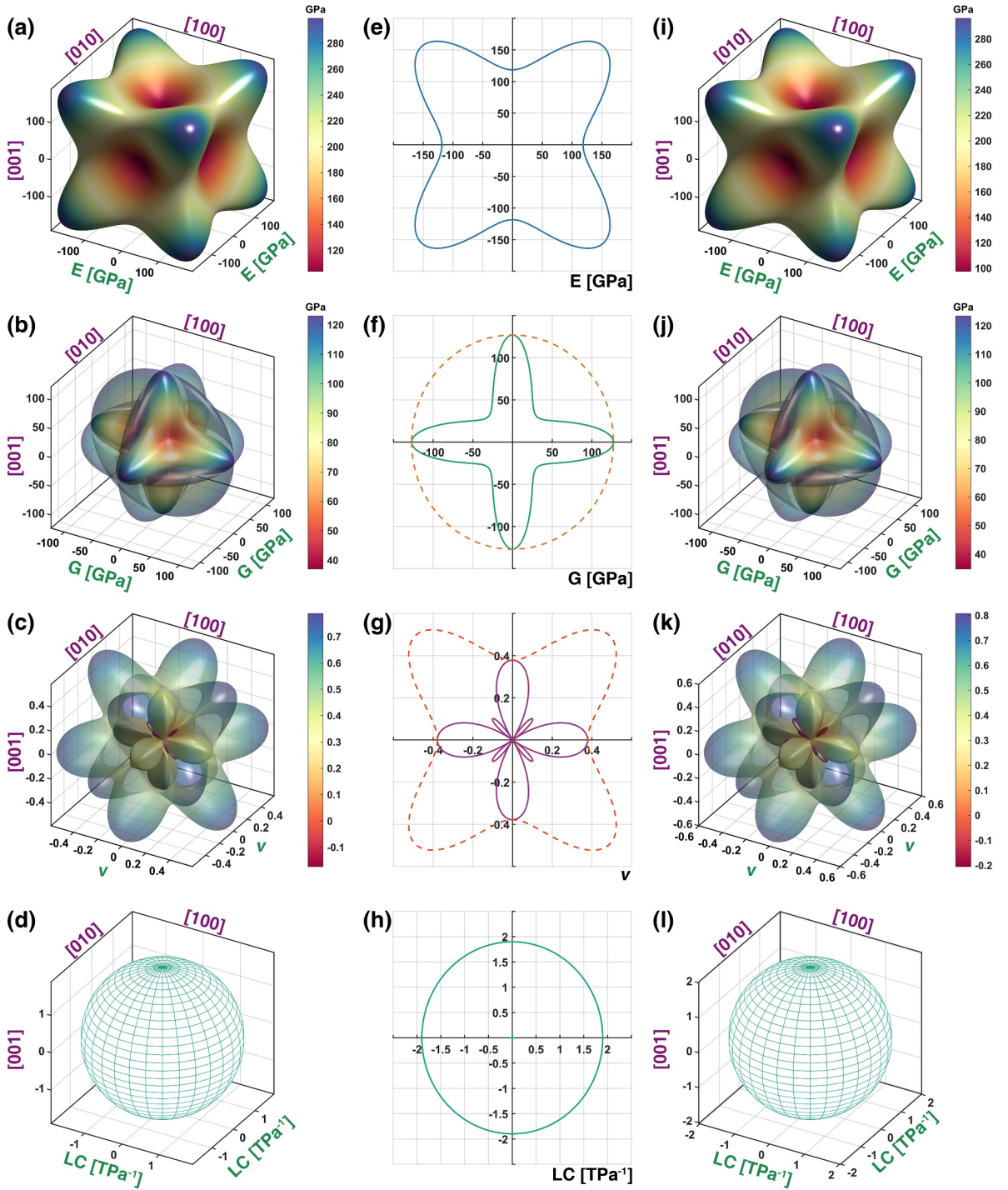
Fig. 7 Elastic properties of the FeNiCr alloy at 293 K determined via *in situ* neutron diffraction measurements (a-h) and DFT calculations (i-l). The magnitude with respect to the directions in three dimensions for: (a)(i) Young's modulus, (b)(j) shear modulus, (c)(k) Poisson's ratio, and (d)(l) linear compressibility, respectively. The maximum and minimum values of shear modulus and Poisson's ratio are represented by two surfaces. The magnitude with respect to directions of XY, XZ, and YZ plane for (e) Young's modulus, (f) shear modulus, (g) linear compressibility, and (h) Poisson's ratio, respectively. The maximum and minimum values of shear modulus and Poisson's ratio are represented by dashed and solid lines, respectively.
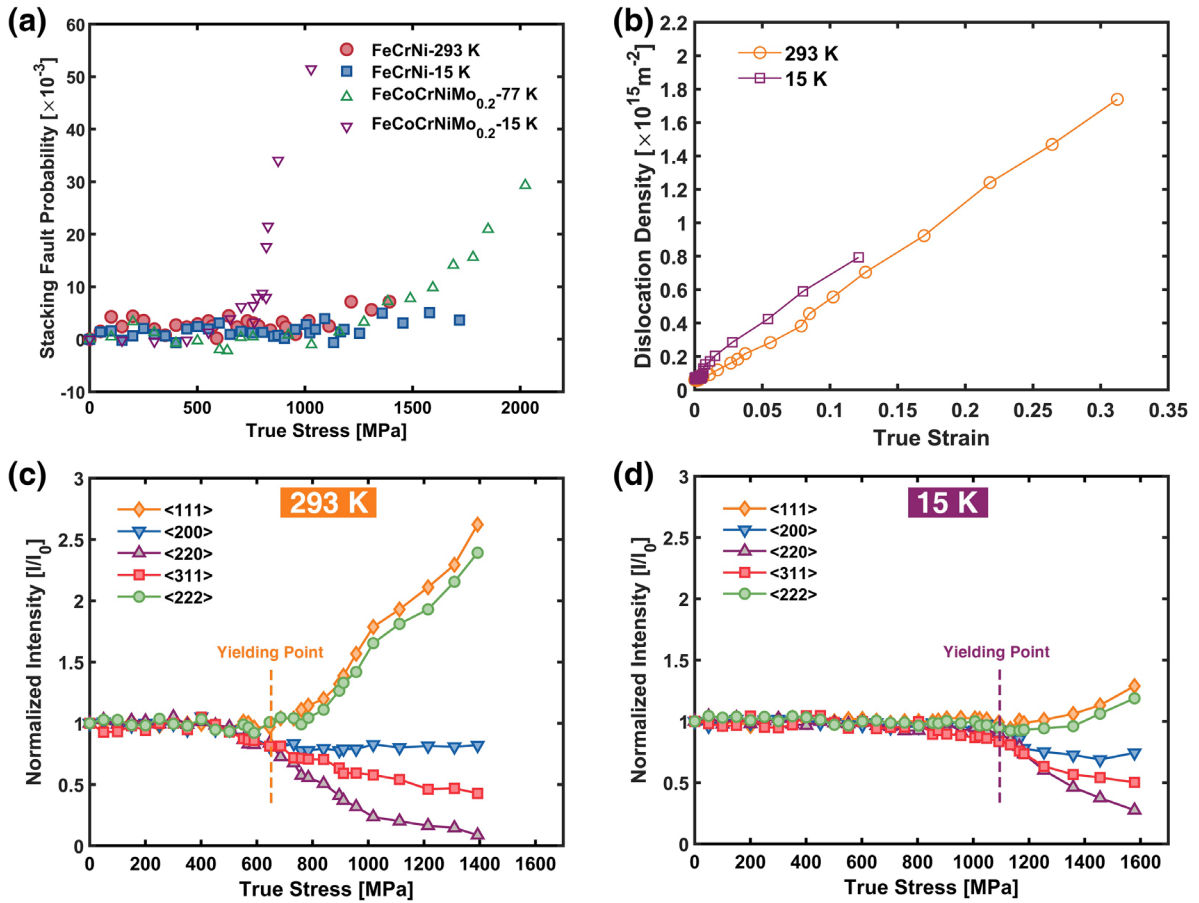
Fig. 8 Microstructure evolution during straining at 293 K and 15 K: (a) comparison of stacking fault probability (SFP) evolution between the FeNiCr alloy and FeCoCrNiMo$_{0.2}$ alloy at different temperatures; (b) dislocation density evolution of the FeNiCr alloy during deformation; The normalized peak intensity evolution of {111}, {200}, {220}, {311}, and {222} of the FeNiCr alloy during deforming at (c) 293 K and (d) 15 K.
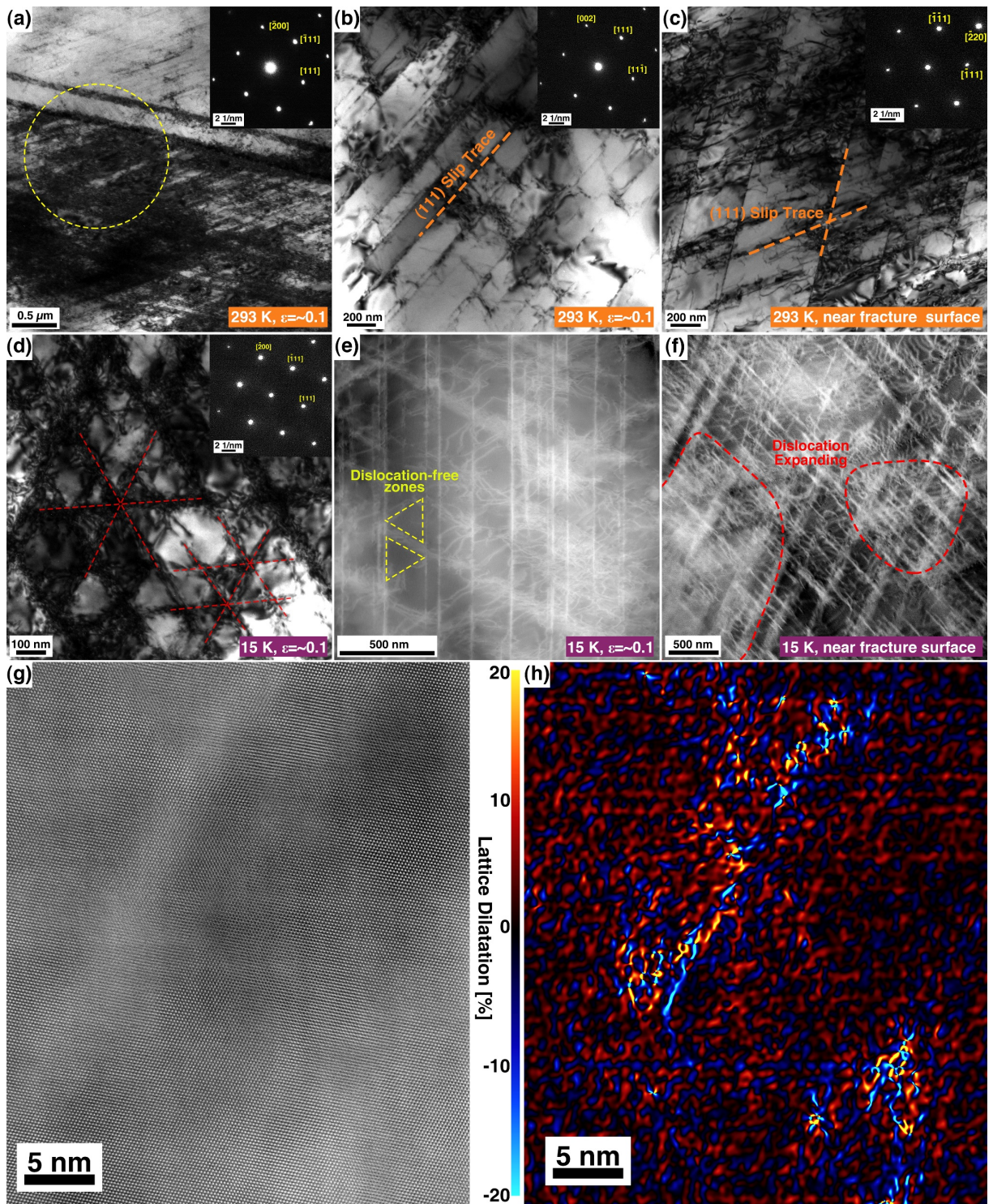
Fig. 9 Deformed microstructure of the alloy at different strain levels and different temperatures, 293 K and 15 K: (a) typical bright-field TEM image (at the strain of ~0.1, 293 K) and corresponding SAED pattern of the area marked by the yellow dashed circle; (b)(c) bright-field TEM images and corresponding SAED patterns at the strain of ~0.1 and near the fracture surface at 293 K, respectively; (d) bright-field TEM image and corresponding SAED pattern at the strain of ~0.1, 15 K; (e)(f) HAADF-STEM images of the deformed structure at the strain of ~0.1 and near the fracture surface at 15 K, respectively; (g) HRTEM image of the dislocation tangling zone in (e); (h) The geometric phase analysis (GPA) conducted on (g).
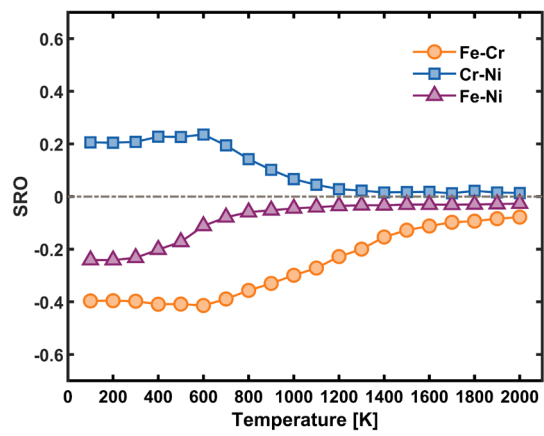
Fig. 10 Dependence of SRO parameters as a function of temperature between the three different pairs in equiatomic FeCrNi alloys.
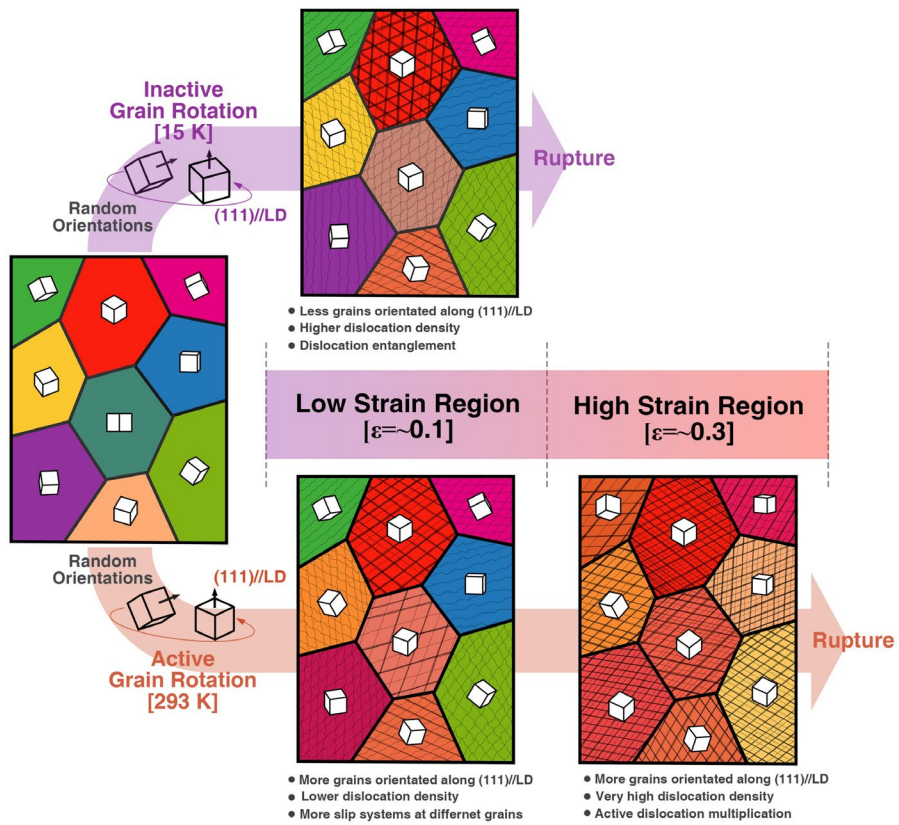
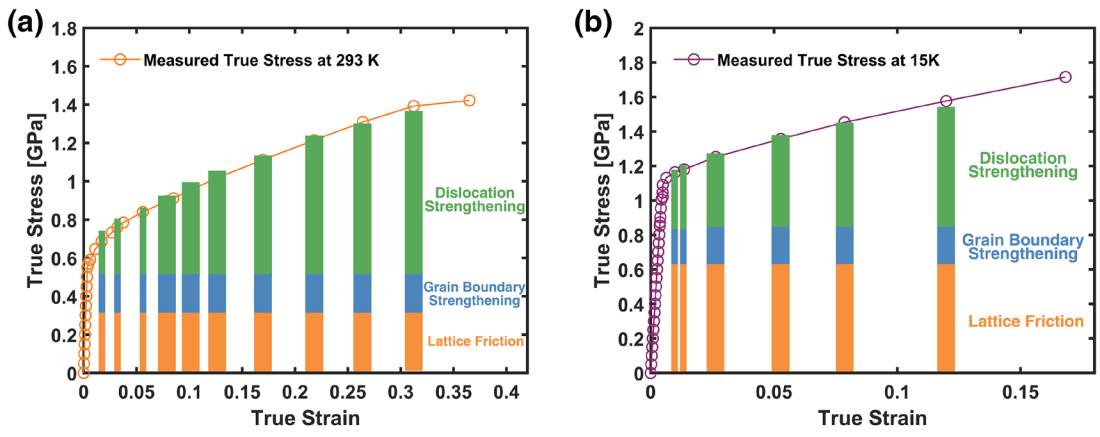**Fig. 11** Schematic illustration of the deformation procedure at 293 and 15 K

Fig. 12 The comparison between the calculated strength originating from different strengthening resources and the measured total flow stress at (a) 293 K and (b) 15 K.

In Situ Neutron Diffraction Unravels Deformation Mechanisms of a Strong and Ductile FeCrNi Medium Entropy Alloy

L. Tang[a], F.Q. Jiang[b], J.S. Wróbel[c], B. Liu[d], S. Kabra[e], R.X. Duan[a], J.H. Luan[f], Z.B. Jiao[g], M.M. Attallah[a], D. Nguyen-Manh[h**], B. Cai[a*]

[a] School of Metallurgy and Materials, University of Birmingham, B15 2TT, United Kingdom
[b] Shenyang National Laboratory for Materials Science, Institute of Metal Research, Chinese Academy of Sciences, Shenyang 110016, China
[c] Faculty of Materials Science and Engineering, Warsaw University of Technology, ul. Wołoska 141, 02-507 Warsaw, Poland
[d] State Key Laboratory for Powder Metallurgy, Central South University, 410083, PR China
[e] ISIS Facility, Rutherford Appleton Laboratory, Didcot OX11 0QX, United Kingdom
[f] Department of Materials Science and Engineering, City University of Hong Kong, Hong Kong, China
[g] Department of Mechanical Engineering, The Hong Kong Polytechnic University, Hong Kong, China
[h] CCFE, United Kingdom Atomic Energy Authority, Abingdon, Oxfordshire OX14 3DB, United Kingdom

*Corresponding authors:
Email addresses: B. Cai: b.cai@bham.ac.uk D. Nguyen: Duc.Nguyen@ukaea.uk

Supplementary Materials

Supplementary Text

Section 1. Single-crystal elastic constants calculation

The diffraction shear moduli based on the Voigt [1], Reuss [2], and Kroner [3] model can be defined with three independent elastic constants, C_{11}, C_{12}, and C_{44}:

$$G_V = \frac{1}{5}(2\mu + 3\eta) \tag{S1}$$

$$G_R = \frac{\mu\eta}{(\eta + 3(\mu - \eta)A_{hkl})} \tag{S2}$$

, in which $A_{hkl} = \dfrac{h^2k^2 + h^2l^2 + k^2l^2}{\left(h^2 + k^2 + l^2\right)^2}$ is the elastic anisotropy factor, $\mu = (C_{11} - C_{12})/2$ and $\eta = C_{44}$ are the shear moduli. While the diffraction shear moduli in the Kroner model can be written with:

$$G_K^3 - \alpha G_K^2 - \beta G_K - \gamma = 0 \tag{S3}$$

, in which G_K is the shear modulus in Kroner model and the coefficients, α, β, and γ are given by:

$$\alpha = \frac{1}{5}(2\mu + 3\eta) - \frac{3}{8}\left\{3K + 4\left[\eta + 3(\mu - \eta)A_{hkl}\right]\right\} \tag{S4}$$

$$\beta = \frac{3}{40}(6K\mu + 9K\eta + 20\mu\eta) - \frac{3}{4}K\left[\eta + 3(\mu - \eta)A_{hkl}\right] \tag{S5}$$

$$\gamma = \frac{3}{4}K\mu\eta \tag{S6}$$

, where $K = (C_{11} + 2C_{12})/3$ is the bulk modulus. Then the reciprocal diffraction elastic moduli ($1/E_{hkl}$ and v_{hkl}/E_{hkl}) can be calculated with:

$$\tag{S7}$$

$$\frac{1}{6G_{hkl}} - \frac{1}{9K} = \frac{v_{hkl}}{E_{hkl}}$$

$$\frac{1}{G_{hkl}} = 2\left(\frac{1}{E_{hkl}} + \frac{v_{hkl}}{E_{hkl}}\right)$$

(S8)

Then least squares estimation was applied to obtain the optimized combination of the three single-crystal elastic constants to minimize the value of a cost function:

$$\chi^2 = \sum_{i=1}^{n}\left((1/E_{hkl})_{mea,i} - (1/E_{hkl})_{mod,i}\right)^2 \bigg/ e_{1,i}^2 + \left((v_{hkl}/E_{hkl})_{mea,i} - (v_{hkl}/E_{hkl})_{mod,i}\right)^2 \bigg/ e_{2,i}^2$$

(S9)

, where n is the number of the reflections, the subscript of "mea" and "mod" represents the values obtained from the experimental measurement and theoretical calculation with Kroner models, respectively. The e_1 and e_2 are the corresponding experimental errors.

The diffraction shear moduli (G_K) in Eq. (S3) can become the isotropic macroscopic shear modulus (G_M) when A_{hkl} equals 0.2. The isotropic macroscopic Young's modulus (E_M) can be obtained via:

$$E_M = \frac{9G_M K}{G_M + 3K}$$

(S10)

The best-fitted single-crystal elastic constants, macroscopic moduli (E_M, G_M, and K_M), and corresponding Poisson's ratio (v_c) at 293 and 15 K are listed in Table S1.

Table S1 The macroscopic moduli fitted with neutron diffraction

Temp. [K]	E_M [GPa]	G_M [GPa]	K_M [GPa]
293	202.3	77.6	175.7
15	213.3	83.7	162.7

Section 2. Stacking fault probability and Stacking fault energy calculation

According to Ref. [4], the shifting of Bragg's diffraction peaks can be influenced by both orientation-dependent macro-strain and stacking faults. Therefore, the experimentally measured lattice strain ($\varepsilon_{hkl,exp}$) can be concurrent effects of the macro-strain ($\varepsilon_{hkl,strain}$) and stacking-fault-induced strain ($\varepsilon_{hkl,sf}$). To determine the influence from stacking faults, a deconvolution procedure was proposed in Ref. [5]:

$$\varepsilon_{hkl,exp} = \varepsilon_{hkl,strain} - \varepsilon_{hkl,sf} = \varepsilon_{hkl,strain} - \frac{\sqrt{3}}{4\pi}\frac{\sum_b \pm(h+k+l)}{(u+b)(h^2+k^2+l^2)}SFP$$

(S11)

, in which u and b are the number of un-broadened and broadened components due to stacking faults [6]. Considering the successive grain families are equivalent in crystallographic directions and their lattice strain evolution should be consistent without the disturbance from stacking faults. This allows us to calculate the SFP via subtracting $\varepsilon_{111,exp}$ from $\varepsilon_{222,exp}$:

$$SFP = \frac{32\pi}{3\sqrt{3}}(\varepsilon_{222,exp} - \varepsilon_{111,exp})$$

(S12)

The stacking fault energy (SFE) of the alloy can then be calculated with the Reed and Schramm equation [7]:

$$SFE = \frac{6.6a_0}{\pi\sqrt{3}} \frac{\langle\varepsilon^2\rangle_{111}}{SFP} (\frac{2C_{44}}{C_{11}-C_{12}})^{-0.37} (\frac{C_{44}+C_{11}-C_{12}}{3}) \tag{S13}$$

, in which $\langle\varepsilon^2\rangle_{111}$ is the mean square microstrain, which is obtained by deconvoluting size and strain broadening effects with the double-Voigt method [8].

Section 3. Dislocation density calculation

The peak broadening effect analysis was carried out to obtain the dislocation density via the modified Williamson-Hall method. The sample and instrumental factors can both contribute to the broadening of diffraction peaks. It is critical to remove instrumental broadening effects (K_{inst}) before further characterization of the microstructure of the samples. The instrument contribution to peak broadening was determined with the stress-free calibrant of CeO_2 and was then subtracted from the measured FWHM (K_{mea}) to obtain the broadening effects of samples (K_{sample}) via [9]:

$$\Delta K_{sample}^2 = \Delta K_{meas}^2 - \Delta K_{inst}^2 \tag{S14}$$

, as a result of deconvolution considering the line profile is very close to Gaussian function as the Gaussian fraction in pseudo-Voigt function is higher than 0.8 for most peaks. Then the dislocation density of the sample was calculated with the modified Williamson-Hall method (W-H), which considers the anisotropy in strain broadening due to the orientation-dependent geometric factors thus a good linear relationship between strain broadening and diffraction vector length can be obtained. In the modified W-H model, sample broadening effect can be ascribed to several factors: average crystalline size (D), stacking faults/twinning probability (β'), and dislocation density (ρ) [10]:

$$\Delta K - \beta'W(g) \cong \frac{a_s}{D} + bM_d\sqrt{\frac{\pi}{2}}\rho(K\overline{C}_{hkl}^{1/2}) + O(K^2\overline{C}) \tag{S15}$$

, where ΔK is the FWHM of each diffraction peak after subtracting instrumental broadening with Eq. (S14). $\beta' = (1.5\alpha + \beta)/a$, where α and β denote the density of stacking fault and twin boundary. $W(g)$ is a scaling factor to obtain the broadening effects of the faults at different peaks [10]. $a_s = 0.9$ is the shape factor for cubic-symmetric spherical crystals, b is the magnitude of the Burger's vector, and M_d is a coefficient depicting the shape of the tail of a profile and was decided by the effective outer cut-off radius of dislocations. $K=1/d$ is the diffraction vector length in TOF neutron diffraction and d is the d-spacing of each reflection. $\overline{C}_{hkl}$ is the averaged contrast factor for each hkl reflection and can be calculated with:

$$\overline{C}_{hkl} = \overline{C}_{h00}\left(1 - q\left[\frac{h^2k^2 + h^2l^2 + k^2l^2}{(h^2+k^2+l^2)^2}\right]\right) \tag{S16}$$

, in which q is a parameter related to the characteristic of edge of screw dislocation and can be determined experimentally. Three elastic constants (C_{11}, C_{12}, and C_{44}) of the alloy obtained at 293 and 15 K in Section 3.5 were applied in the calculation of $\overline{C}_{h00}$, the average contrast factor of $\{h00\}$ reflection, which is also dependent on the ratio of screw/edge dislocation and their contrast factors of $\{h00\}$ reflections ($C_{h00,i}$, the subscript i means the dislocation type). The C_{h00} of pure screw/edge dislocations can be determined with:

$$C_{h00i} = a_i^{c_{h00}} \left[1 - \exp\left(\frac{-A_i}{b_i^{c_{h00}}} \right) \right] + c_i^{c_{h00}} A_i + d_i^{c_{h00}} \tag{S17}$$

, where $A_i = \dfrac{2C_{44}}{C_{11} - C_{12}}$ is the elastic anisotropy parameter. According to Ref. [11], the four coefficients of $a_i^{c_{h00}}$, $b_i^{c_{h00}}$, $c_i^{c_{h00}}$, and $d_i^{c_{h00}}$ are dependent with two parameters (C_{11}/C_{44} and A_i) strongly related to the elastic constants. The low SFP results shown in Fig. 6c and 6d indicate that the very low density of stacking faults/twinning were introduced at both temperatures, hence we do not consider the faults-induced broadening effects ($\beta'W(g)$) in the peak broadening analysis. Then the screw/edge ratio ranging from 0 to 1 was used in Eq. (S15) to fit the modified W-H plots and the C_{hkl} gives the highest R-square value was chosen to evaluate the dislocation density [12]. ΔK and K of five reflections of (111), (200), (220), (311), and (222) were used for fitting the modified W-H plots at 293 and 15 K (Fig. S1a and S1b) with very high R-square values (above 0.9).
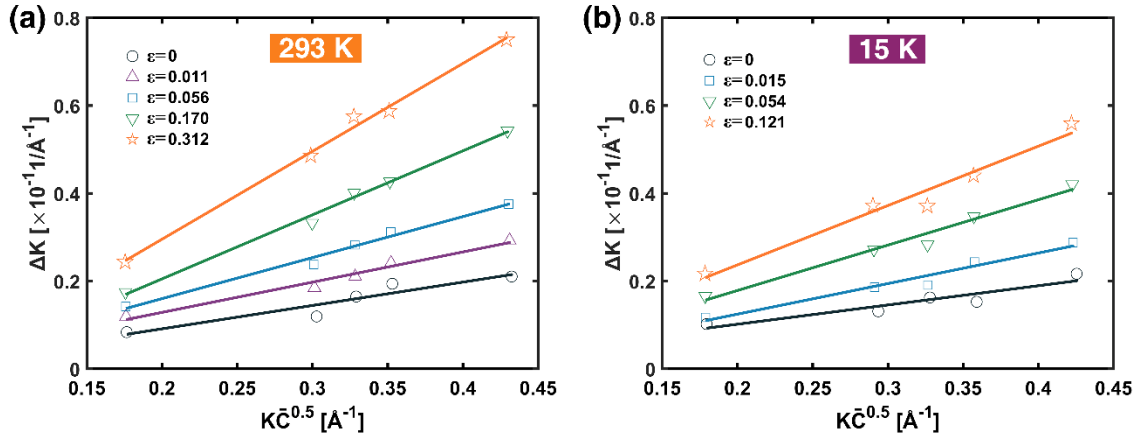

Fig. S1 Modified Williamson Hall plots of the alloy during deforming at (a) 293 K and (b) 15 K.

Section 4. Elastic modulus calculation from DFT

In this study, we applied the method of calculation of the anisotropy of Young's modulus and Poisson's ratio proposed by Wróbel et al. [13] in order to investigate the anisotropy of elastic properties. The variation of Young's modulus and Poisson's ratio as a function of the orientation with respect to the crystal lattice required the calculation of the fourth-order elastic compliance tensor, S_{ijkl}, which was determined via inversion of the second-order elasticity tensor, C_{ij}. The Young's modulus, $E_{(hkl)}$, and the average Poisson ratio, $\upsilon_{(hkl)}$, along a direction normal to the lattice plane system described with Miller indices (hkl) (in amorphous structure these Miller indices describe spatial coordinates) are given as:

$$E_{(hkl)} = \frac{1}{s'_{3333}} \tag{S18}$$

$$\upsilon_{(hkl)} = -\frac{s'_{1133} + s'_{2233}}{2s'_{3333}} \tag{S19}$$

Here, s'_{ijkl} are components of the compliance tensor in the new reference system (the new lattice plane system rotated from the original one and described with Miller indices (hkl)) written in fourth-

order tensor notation and transformed from the compliances of the crystal, s_{mnop}, in the original cubic crystal axes. Hence

$$s'_{ijkl} = a_{im}a_{jn}a_{ko}a_{lp}s_{mnop} \tag{S20}$$

where a_{im}, a_{jn}, a_{ko}, and a_{lp} are the transformation matrices [14]. The transformation matrix, a_{rt}, from the original cubic crystal axes to the new lattice plane system described with Miller indices (hkl) can be expressed explicitly in terms of Miller indices of this plane [15].

$$(a_{rt}) = \begin{bmatrix} \dfrac{hl}{\sqrt{h^2+k^2}\sqrt{h^2+k^2+l^2}} & \dfrac{kl}{\sqrt{h^2+k^2}\sqrt{h^2+k^2+l^2}} & -\dfrac{\sqrt{h^2+k^2}}{\sqrt{h^2+k^2+l^2}} \\ -\dfrac{k}{\sqrt{h^2+k^2}} & \dfrac{h}{\sqrt{h^2+k^2}} & 0 \\ \dfrac{h}{\sqrt{h^2+k^2+l^2}} & \dfrac{k}{\sqrt{h^2+k^2+l^2}} & \dfrac{l}{\sqrt{h^2+k^2+l^2}} \end{bmatrix} \tag{S21}$$

where h, k, l are the direction cosines.

In the method presented here, the transformation matrix, a_{rt}, is calculated for each orientation (chosen from a uniformly distributed set of directions) and $E_{(hkl)}$ and $\upsilon_{(hkl)}$ are obtained from Eqs. (S18-S20). A convenient representation of anisotropy is a plot of Young's modulus and Poisson's ratio surfaces. Each point on a given surface represents the magnitude of Young's modulus in the direction of a vector from the origin to a given point on the surface. In this way, the surfaces map out how Young's modulus varies with direction.

In order to obtain the theoretical values of elastic moduli for polycrystalline materials, the Reuss-Voigt-Hill method has been employed with the following equations [16]:

$$B_{Voigt} = \frac{1}{9}[c_{11} + c_{22} + c_{33} + 2(c_{12} + c_{23} + c_{13})] \tag{S22}$$

$$G_{Voigt} = \frac{1}{15}[c_{11} + c_{22} + c_{33} - c_{12} - c_{23} - c_{13} + 3(c_{44} + c_{55} + c_{66})] \tag{S23}$$

$$E_{Voigt} = \frac{9B_{Voigt}G_{Voigt}}{3B_{Voigt} + G_{Voigt}} \tag{S24}$$

$$B_{Reuss} = [s_{11} + s_{22} + s_{33} + 2(s_{12} + s_{23} + s_{13})]^{-1} \tag{S25}$$

$$G_{Reuss} = 15[4(s_{11} + s_{22} + s_{33} - s_{12} - s_{23} - s_{13}) + (s_{44} + s_{55} + s_{66})]^{-1} \tag{S26}$$

$$E_{Reuss} = \frac{9B_{Reuss}G_{Reuss}}{3B_{Reuss} + G_{Reuss}} \tag{S27}$$

Table S2 Elastic constants and moduli predicted by DFT calculations and compared with experimental data.

	FeCrNi	DFT 2000 K	DFT 2000 K	DFT 300 K	DFT 300 K	In situ Exp. 293 K	In situ Exp. 15 K
	Symmetry	$P1$	$P1$	$Pnnm$	$Pnnm$		
	K-points	4×4×4	4×4×4	4×4×4	6×6×6		
		Relaxed	Unrelaxed	Relaxed	Relaxed		
Elastic Constant [GPa]	C_{11}	210.79	222.45	239.41	237.44	225	220
	C_{12}	141.19	134.8	117.01	116.4	151	134
	C_{13}	136.06	142.6	136.48	137.24	-	-
	C_{22}	200.47	213.16	231.37	229.99	-	-
	C_{23}	127.42	132.09	109.34	108.92	-	-
	C_{33}	206.05	218.31	257.46	259.19	-	-
	C_{44}	123.42	125.36	163.14	163.46	123	127
	C_{55}	122.36	138.84	143.22	142.18	-	-
	C_{66}	122.19	131.67	141.19	140.99	-	-
	$(C_{11}+C_{22}+C_{33})/3$	205.8	218.0	242.7	242.2	-	-
	$(C_{12}+C_{13}+C_{23})/3$	134.9	136.5	120.9	120.9	-	-
	$(C_{44}+C_{55}+C_{66})/3$	122.7	132.0	149.2	148.9	-	-
	C' (average)	35.4	40.7	60.9	60.7	37.0	43.0
Young's Modulus [GPa]	E_{min}	94.2	111.02	148.21	146.05	103.71	118.55
	E_{max}	292.52	311.98	341.52	340.82	299.1	302.27
	E_{av}	180.83	199.81	248.02	247.12	187.95	201.8
	E_{max}/E_{min}	3.105	2.81	2.304	2.334	2.884	2.55
	SD	50.77	52.26	48.63	48.78	50.93	48.31
	SD/E_{av} (%)	28.08	26.15	19.61	19.74	27.09	23.94
Poisson's Ratio	P_{min}	0.1914	0.1823	0.1449	0.1447	0.2162	0.1903
	P_{max}	0.4196	0.3985	0.3569	0.3572	0.4016	0.3785
	P_{av}	0.3093	0.2962	0.2429	0.2433	0.3216	0.2932
	P_{max}/P_{min}	2.192	2.186	2.463	2.468	1.856	1.989
	SD	0.055	0.0539	0.0534	0.0539	0.04016	0.0496
	SD/P_{av} (%)	17.78	18.21	21.97	22.14	15.08	16.93
Polycrystalline Moduli [GPa]	$B_{(VRH)}$	158.33	163.53	161.09	160.77	175.65	162.67
	$G_{(VRH)}$	74.57	82.45	103.62	103.27	76.17	82.35
	$E_{(VRH)}$	192.64	211.12	255.64	254.82	199.06	210.9

Section 5. Calculation of phase formation parameters

Solid-solution phases are the more desirable in multi-component alloys as their promising mechanical properties. There are several criteria in predicting the constituent phases of the multi-component alloys. According to Ref. [17], the Gibbs free energy difference between solid- and liquid-state (ΔG_{mix}) can be expressed with:

$$\Delta G_{mix} = \Delta H_{mix} - T\Delta S_{mix} \qquad (S28)$$

, in which T is the absolute temperature, ΔS_{mix} and ΔH_{mix} are the entropy of mixing and the enthalpy of mixing, respectively. For a random multi-component alloy with n elements, they can be calculated with [18,19]:

$$\Delta S_{mix} = -R\sum_{i}^{n} c_i \ln c_i \qquad (S29)$$

$$\Delta H_{mix} = \sum_{i=1, i \neq j}^{n} \Omega_{ij} c_i c_j \qquad (S30)$$

, in which R=8.314 JK^{-1}mol^{-1} is the gas constant, c_i is the mole percent of component i. $\Omega_{ij} = 4\Delta H_{AB}^{mix}$ is the regular solution interaction parameter between two elements (ith and jth). ΔH_{AB}^{mix} is the mixing enthalpy of binary alloys, its values can be calculated with the Miedema macroscopic model in Ref. [20]. The multi-component alloys preferably form solid-solution phases if their ΔG_{mix} drops to the lowest level comparing with other possible phases. According to Ref. [19], the large absolute value of ΔH_{mix} can impede the solid-solution formation. When ΔH_{mix} approaches zero, the different elements can randomly distribute among the matrix and form solid-solution phase. On the other hand, increasing ΔS_{mix} can effectively lower ΔG_{mix} and lower the tendency of ordering and segregation of alloy elements.
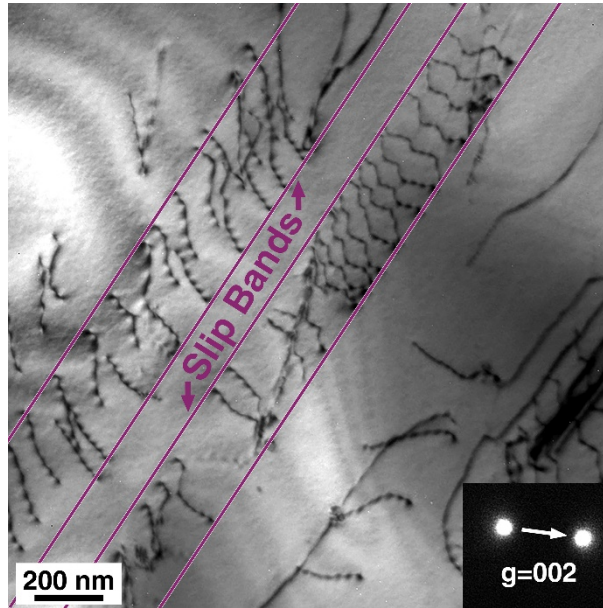
Section 6 TEM observation

Fig. S2 Two-beam bright-field TEM image of a slightly deformed sample shows the representative wavy configuration of dislocation in the MEA

References

[1] W. Voigt, Lehrbuch Der Kristallphysik, Teubner Leipzig, 1928.

[2] A. Reuss, ZAMM - J. Appl. Math. Mech. / Zeitschrift Für Angew. Math. Und Mech. 9 (1929) 49–58.

[3] A. Morawiec, Phys. Status Solidi 154 (1989) 535–541.

[4] J.S. Jeong, Y.M. Koo, I.K. Jeong, S.K. Kim, S.K. Kwon, Mater. Sci. Eng. A 530 (2011) 128–134.

[5] B.E. Warren, X-Ray Diffraction, Courier Corporation, 1990.

[6] G. Caglioti, A. t Paoletti, F.P. Ricci, Nucl. Instruments 3 (1958) 223–228.

[7] R.P. Reed, R.E. Schramm, J. Appl. Phys. 45 (1974) 4705–4711.

[8] D. Balzar, Microstruct. Anal. from Diffr. (1999) 44.

[9] L. Tang, L. Wang, M. Wang, H. Liu, S. Kabra, Y. Chiu, B. Cai, Acta Mater. 200 (2020) 943–958.

[10] T. Ungár, S. Ott, P.G. Sanders, A. Borbély, J.R. Weertman, Acta Mater. 46 (1998) 3693–3699.

[11] T. Ungár, I. Dragomir, Á. Révész, A. Borbély, J. Appl. Crystallogr. 32 (1999) 992–1002.

[12] X. Zhang, M. Li, J.S. Park, P. Kenesei, J. Almer, C. Xu, J.F. Stubbins, Acta Mater. 126 (2017) 67–76.

[13] J. Wróbel, L.G. Hector, W. Wolf, S.L. Shang, Z.K. Liu, K.J. Kurzydłowski, J. Alloys Compd. 512 (2012) 296–310.

[14] J.F. Nye, Physical Properties of Crystals: Their Representation by Tensors and Matrices, Oxford university press, 1985.

[15] J. Wróbel, L.G. Hector, W. Wolf, S.L. Shang, Z.K. Liu, K.J. Kurzydłowski, J. Alloys Compd. 512 (2012) 296–310.

[16] R. Hill, Proc. Phys. Soc. Sect. A 65 (1952) 349–354.

[17] A. Takeuchi, A. Inoue, Mater. Sci. Eng. A 304–306 (2001) 446–451.

[18] J.-W. Yeh, JOM 65 (2013) 1759–1771.

[19] A.R. Miedema, P.F. de Châtel, F.R. de Boer, Phys. B+C 100 (1980) 1–28.

[20] M. Zhang, L.G. Hector, Y. Guo, M. Liu, L. Qi, Comput. Mater. Sci. 165 (2019) 154–166.